Calhoun: The NPS Institutional Archive

DSpace Repository

Theses and Dissertations | 1. Thesis and Dissertation Collection, all items

1986

Measurements of the microscopic properties contributing to photorefraction in barium titanate.

Unal, Gazanfer.

http://hdl.handle.net/10945/21970

Downloaded from NPS Archive: Calhoun

http://www.nps.edu/library

Calhoun is the Naval Postgraduate School's public access digital repository for research materials and institutional publications created by the NPS community. Calhoun is named for Professor of Mathematics Guy K. Calhoun, NPS's first appointed -- and published -- scholarly author.

Dudley Knox Library / Naval Postgraduate School
411 Dyer Road / 1 University Circle
Monterey, California USA 93943

DUDLEY KNOX LIBRARY
NAVAL POSTGRADUATE SCHOOL
MONTEREY, CALIFORNIA 93943-5002

NAVAL POSTGRADUATE SCHOOL
Monterey, California

THESIS

MEASUREMENTS OF THE MICROSCOPIC PROPERTIES CONTRIBUTING TO PHOTOREFRACTION IN $BATIO_3$

by

Gazanfer Unal

December 1986

Thesis Advisor Donald L. Walters

Approved for public release; distribution is unlimited.

T233682

URITY CLASSIFICATION OF THIS PAGE

REPORT DOCUMENTATION PAGE

REPORT SECURITY CLASSIFICATION UNCLASSIFIED	1b RESTRICTIVE MARKINGS
SECURITY CLASSIFICATION AUTHORITY	3 DISTRIBUTION / AVAILABILITY OF REPORT Approved for public release; distribution is unlimited
DECLASSIFICATION / DOWNGRADING SCHEDULE	
PERFORMING ORGANIZATION REPORT NUMBER(S)	5 MONITORING ORGANIZATION REPORT NUMBER(S)
NAME OF PERFORMING ORGANIZATION Naval Postgraduate School 6b OFFICE SYMBOL (If applicable) 61	7a NAME OF MONITORING ORGANIZATION Space Defense Initiative Organization (SDIO/DE)
ADDRESS (City, State, and ZIP Code) Monterey, California 93943-5000	7b ADDRESS (City, State, and ZIP Code) 1717 H Street Washington, D.C. 20301
NAME OF FUNDING / SPONSORING ORGANIZATION Rome Air Develop-nt Center (RADC) Dr. Don Hanson 8b OFFICE SYMBOL (If applicable) OCSP	9 PROCUREMENT INSTRUMENT IDENTIFICATION NUMBER FQ761960025
ADDRESS (City, State, and ZIP Code) Griffiss, AFB, New York 13441	10 SOURCE OF FUNDING NUMBERS PROGRAM ELEMENT NO / PROJECT NO / TASK NO / WORK UNIT ACCESSION NO

TITLE (Include Security Classification)
MEASUREMENTS OF THE MICROSCOPIC PROPERTIES CONTRIBUTING TO PHOTOREFRACTION IN BARIUM TITANATE

PERSONAL AUTHOR(S)
Unal Gazanfer

13a TYPE OF REPORT	13b TIME COVERED	14 DATE OF REPORT (Year, Month, Day)	15 PAGE COUNT
Master's Thesis	FROM ____ TO ____	1986 December	82

SUPPLEMENTARY NOTATION
This work was supported under RADC MIPR FQ761960025 Job order 622716RSUWE

COSATI CODES		
FIELD	GROUP	SUB-GROUP

18 SUBJECT TERMS (Continue on reverse if necessary and identify by block number)
Phase Conjugation Barium Titanate
Photorefraction

9 ABSTRACT (Continue on reverse if necessary and identify by block number)

The photorefractive effect is a nonlinear optical phenomena that can produce phase conjugate (complex conjugate) reflection of visible light in a crystalline solid. Very little is known about the microscopic origin of photorefraction; consequently this thesis investigates the following microscopic parameters of barium titanate ($BaTiO_3$): the quantum efficiency, charge transport length and the carrier generation rate both theoretically and experimentally. $BaTiO_3$ was chosen because it is a highly nonlinear crystal with large electrooptic coefficients and therefore, is a very efficient photorefractive material.

20 DISTRIBUTION / AVAILABILITY OF ABSTRACT ☒ UNCLASSIFIED/UNLIMITED ☐ SAME AS RPT ☐ DTIC USERS	21 ABSTRACT SECURITY CLASSIFICATION UNCLASSIFIED
22a NAME OF RESPONSIBLE INDIVIDUAL D. L. Walters	22b TELEPHONE (Include Area Code) 408-646-2267 22c OFFICE SYMBOL 61We

DD FORM 1473, 84 MAR 83 APR edition may be used until exhausted
All other editions are obsolete

SECURITY CLASSIFICATION OF THIS PAGE

☆ U.S. Government Printing Office 1986—606-24

Approved for public release; distribution is unlimited.

Measurements of the Microscopic Properties Contributing to Photorefraction in $BaTiO_3$

by

Gazanfer Unal
Lieutenant Junior Grade, Turkish Navy
B.S., Naval Academy Istanbul, 1980

Submitted in partial fulfillment of the
requirements for the degree of

MASTER OF SCIENCE IN PHYSICS

from the

NAVAL POSTGRADUATE SCHOOL
December 1986

ABSTRACT

The photorefractive effect is a nonlinear optical phenomena that can produce phase conjugate (complex conjugate) reflection of visible light in a crystalline solid. Very little is known about the microscopic origin of photorefraction; consequently this thesis investigates the following microscopic parameters of barium titanate ($BaTiO_3$): the quantum efficiency, charge transport length and the carrier generation rate both theoretically and experimentally. $BaTiO_3$ was chosen because it is a highly nonlinear crystal with large electrooptic coefficients and therefore, is a very efficient photorefractive material.

TABLE OF CONTENTS

I. INTRODUCTION 9

II. THEORY OF PHOTOREFRACTION 11

A. THE STRUCTURE OF THE $BATIO_3$ 11

B. DIELECTRIC PROPERTIES OF $BATIO_3$ 13

1. The spontaneous polarization 13

2. Dielectric constant of $BaTiO_3$ 15

3. General ferroelectric properties of $BaTiO_3$ 16

4. The pyroelectric effect 18

C. BULK PHOTOVOLTAIC EFFECT 19

D. SEMICONDUCTOR PROPERTIES OF $BATIO_3$ 24

E. CHARGE TRANSPORT IN $BATIO_3$ 28

F. ELECTROOPTIC EFFECT 34

G. PHOTOREFRACTIVE EFFECT IN $BATIO_3$ 37

H. DERIVATION OF THE QUANTUM EFFICIENCY OF $BATIO_3$ 41

III. EXPERIMENTAL OBSERVATIONS 47

A. ABSORTION COEFFICIENT MEASUREMENTS 47

1. Purpose of this experiment 47

2. Procedure 47

3. Results of the experiments 49

4. Interpretation of the results 50

B. PHOTOCURRENT MEASUREMENT EXPERIMENTS 57

1. Purpose of this experiment 57

2. Procedure 58

3. Results of the experiments 59

4. Interpretation of the results 60

C. BEAM-COUPLING EXPERIMENTS 65

1. Purpose of this experiment 65

2. Procedure 65
3. Results of the experiments 66
4. Interpretation of the results 68
D. CALCULATION OF THE QUANTUM EFFICIENCY OF $BATIO_3$ 70
E. DISCUSSIONS 76
IV. CONCLUSIONS 77
LIST OF REFERENCES 79
INITIAL DISTRIBUTION LIST 81

LIST OF TABLES

1. MICROSCOPIC PARAMETERS OF $BATIO_3$ 46

LIST OF FIGURES

2.1 Unit cell of $BaTiO_3$ 11
2.2 Unit cells of the four phases of $BaTiO_3$ [Ref.2] 12
2.3 Ionic motions in $BaTiO_3$ [Ref.3] 15
2.4 Temperature dependence of spontaneous polarization [Ref.6] 16
2.5 Dielectric constant of $BaTiO_3$ as a function of temperature T [Ref.2] 17
2.6 Spontaneous polarization vs temperature [Ref.6] 17
2.7 p(T) from P_s vs T [Ref.8] 19
2.8 Photovoltage vs temperature [Ref.13] 20
2.9 Charge distributions of intrinsic BPVE [Ref.16] 21
2.10 Donors-Acceptors in a ferroelectric semiconductor [Ref.19] 24
2.11 Relative contribution of electrons and holes to the photoconductivity [Ref.18] 26
2.12 Oxygen vacancies as photorefractive centres [Ref.19] 27
2.13 Energy levels of $B^{n+}\ O_6^{-12+n}$ clusters in $BaTiO_3$ [Ref.18] 28
2.14 Band model of charge transport in $BaTiO_3$ [Ref.18] 29
2.15 Redistribution of charges under illumination [Ref.19] 30
2.16 Formation of interference pattern [Ref.27] 37
2.17 Photorefraction due to beam-coupling [Ref.18] 38
2.18 Polarization surface charges 41
3.1 Measured absorption spectrum of $BaTiO_3$, $\underline{E} \perp c$, $\underline{K} \parallel c$ 49
3.2 Measured absorption spectrum of $BaTiO_3$, $\underline{E} \perp c$, $\underline{K} \parallel c$ 50
3.3 Measured absorption spectrum of $BaTiO_3$, $\underline{E} \perp c$, $\underline{K} \perp c$ 51
3.4 Measured absorption spectrum of $BaTiO_3$, $\underline{E} \perp c$, $\underline{K} \perp c$ 52
3.5 Measured absorption spectrum of $BaTiO_3$, $\underline{E} \parallel c$, $\underline{K} \perp c$ 53
3.6 Measured absorption spectrum of $BaTiO_3$, $\underline{E} \parallel c$, $\underline{K} \perp c$ 54
3.7 Measured absorption spectrum of $BaTiO_3$ at IR region 55
3.8 IR active normal vibrations of a TiO_6 octahedron [Ref.33] 57
3.9 Experimental set up 58
3.10 Measured photocurrent along +c axis 59

3.11 Measured photocurrent along -c axis 60
3.12 i_{py} (the pyroelectric current) versus incident power 61
3.13 i_{ph} (SCPVC) versus incident power 62
3.14 Experimental set-up for beam-coupling. 66
3.15 The fractional energy transfer (F) at λ = 488nm 67
3.16 The fractional energy transfer (F) at λ = 457.9nm 68
3.17 Diffraction efficiency vs wavelength 69
3.18 Photorefractive absorption coefficient of $BaTiO_3$ 72
3.19 Anisotropy constant of $BaTiO_3$ 73
3.20 Phase shift angle between gratings 74
3.21 Quantum efficiency of $BaTiO_3$ 75
4.1 Intensity vs the index of refraction change [Ref.39] 77

I. INTRODUCTION

Photorefraction is the change in the index of refraction of an optical material under intense laser illumination. Photorefraction was originally discovered in nonlinear optical investigations of $LiNbO_3$ [Ref. 1]. At that time, it was interpreted as optical damage in the crystal due to undesirable scattering and decollimation of laser light. Later, Kukhtarev et al. [Ref. 2] explained it as a three step process: 1) Under laser illumination, optical excitation of electrons and holes occurs. Electrons move from donor sites in the crystal to the conduction band and holes move from acceptor sites to the valence band. 2) The photo-excited carriers migrate from the illuminated regions to the dark regions under the influence of diffusion, drift in an external electric field, and the bulk photovoltaic effect (BPVE). The charge transport mechanisms separate charge pairs from each other and this produces a space-charge field, inside the crystal. 3) This induced space-charge electric field alters the index of refraction of the crystal via an electrooptic (Pockel) effect.

If two or more beams intersect to form an interference pattern within a crystal, the standing wave pattern can produce a three dimensional volume hologram. This grating can then produce a phase conjugate reflection (complex conjugate of the E-M field) of the incident beam that is important in phase conjugation studies. In addition, the grating is responsible for a transfer of energy between the two intersecting beams. This process is called two beam coupling.

Photorefraction depends on the following parameters: a) the amount of light absorbed by the crystal, b) the density and type of impurities in the crystal, c) the type of carriers and the charge transport mechanisms, d) and the magnitude of the electrooptic coefficients.

$BaTiO_3$ was chosen for investigation since it is a ferroelectric crystal that has large nonlinear electrooptic coefficients. Consequently, $BaTiO_3$ has a large diffraction efficiency that makes it ideal for phase conjugation and photorefraction applications.

Photorefractive materials such as, $BaTiO_3$, $LiNbO_3$, $LiTaO_3$ and bismuth silicon oxide are finding many applications. They can be used as optical phase conjugation elements and as volume holographic optical elements. Optical phase conjugation is used to correct static and dynamic distortions in optical systems. Since

the phase conjugate beam is a complex conjugate of the incident beam wave, it is in effect a time reversed replica of the incident beam. Consequently, phase distortions imposed by propagation through a perturbing media such as the atmosphere will be undone when the phase conjugate wave returns through the medium along the same optical path. In addition, phase conjugation is used to improve laser resonators, in atmospheric communication networks and in image amplifying systems. Since the interference pattern represents a volume hologram, photorefractive materials are used as volume holographic storage media in optical data processing systems.

In order to understand the source of the photorefractive effect in $BaTiO_3$, the quantum efficiency and the number of photo-excited carriers produced per absorbed photon, were needed. Consequently, this thesis attempts to determine the quantum efficiency, the charge transport length and carrier generation rate in $BaTiO_3$. The quantum efficiency was unknown at the start of this thesis. To determine the quantum efficiency, the photorefractive absorption coefficient was needed, in addition to the pyroelectric current, the bulk photovoltaic current and the phase shift angle between the hologram grating and intensity pattern. Chapter II contains the main aspects of the theories for spontaneous polarization, the ferroelectric properties, the pyroelectric effect, the bulk photovoltaic effect, the semiconductor properties, the charge transport mechanisms, the electrooptical and photorefractive effect in $BaTiO_3$. In addition, the theoretical section contains an expression for the quantum efficiency in terms of experimentally measurable parameters. Chapter III presents the experimental observations.This includes spectrophotometer absorption measurements of $BaTiO_3$ for different wavelengths and orientations of polarized light. In addition the pyroelectric effect, the change in the spontaneous polarization, versus temperature was used to measure, indirectly the absorption coefficient. The quantum efficiency was ultimately determined from the pyroelectric absorption coefficients and the phase shift angle determined from the beam coupling measurements. Chapter IV summarizes the results of this thesis.

II. THEORY OF PHOTOREFRACTION

A. THE STRUCTURE OF THE $BATIO_3$

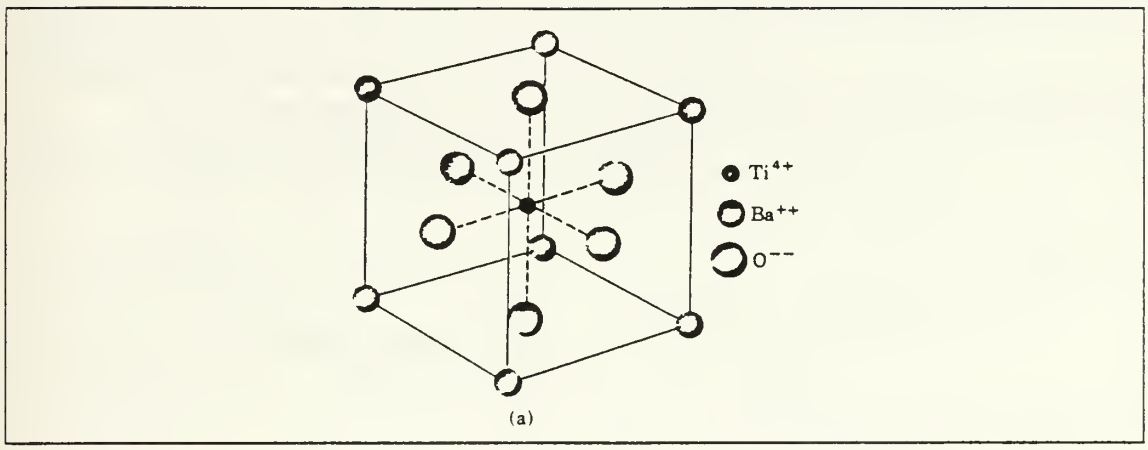

Figure 2.1 Unit cell of $BaTiO_3$.

Figure 2.1 shows that a unit cell of $BaTiO_3$ contains a Ba^{2+} ion on each corner of the cube, an O^{2-} ion at the center of each face and a Ti^{4+} ion at the center of the cube. $BaTiO_3$ has four different unit cell structures for four phases [Ref. 3]. It has a cubic symmetry above the Curie temperature 118°C; and it is nonpolar, centrosymmetric and nonpiezoelectric with point group m3m. In the cubic phase, $BaTiO_3$ is not ferroelectric, but has pyroelectric properties and it is paraelectric. The crystal has tetragonal symmetry between 118°C and 5°C with point group 4mm. This phase is polar and the four fold axis is the polar direction known as the c-axis. In this phase, the crystal has ferroelectric, pyroelectric and semiconductor properties, which permits photorefraction. A tetragonal unit cell results from distortion of the nonpolar cubic cell; one of the cube edges stretches to become the tetragonal c-axis, the other two edges compress to become the tetragonal a-axis. At 5°C, another phase transition occurs and $BaTiO_3$ becomes orthorhombic with point group mm. In this phase, it is still ferroelectric but the direction of spontaneous polarization is no longer the original cubic <100> direction as it was for the cubic and tetragonal phases. Instead, it is parallel to one of the original cubic <110> directions. The orthorhombic unit cell arises from distortion of the cubic cell; one of the face diagonals is elongated to

become the orthorhombic a-axis, the two other face diagonals are compressed to become the orthorhombic b-axis. The last transition is at -90°C and the unit cell becomes rhombohedral with point group 3m. In this phase, the polar axis is parallel to one of the original cubic <111> directions. The rhombohedral unit cell results from the elongation of the original cubic cell along one of the body diagonals. This section can be summarized in Figure 2.2 .

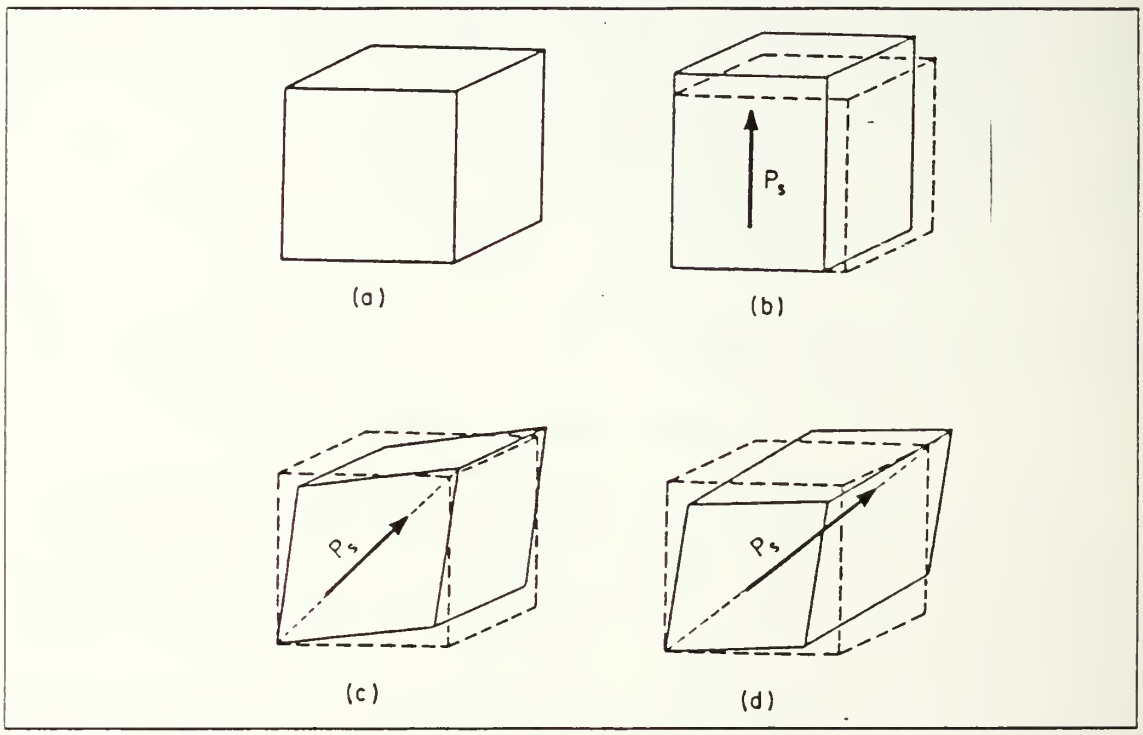

Figure 2.2 Unit cells of the four phases of $BaTiO_3$ [Ref.2].

(a) The cubic phase is stable above 118°C, (b) Tetragonal is stable between 118°C and 5°C, (c) Orthorhombic is stable between 5°C and -90°C, (d) Rhombohedral is stable below -90°C.

The dashed lines in Figure 2.2 (b), (c) and (d) shows the original cubic cell; P_S is the spontaneous polarization vector.

B. DIELECTRIC PROPERTIES OF $BATIO_3$

1. The spontaneous polarization

In general there are three types of polarization. 1) Dipolar polarization arises from molecules which have dipole moments that can change their orientation when the field is applied. This type of polarization is important in the UHF and microwave region of the spectrum. 2) Ionic polarization results from the displacements of the ions with respect to each other and is important in the infrared region of the spectrum. 3) Electronic polarization, which arises from the distortion of the electron shell relative to a nucleus, is dominant in the optical part of the spectrum.

In an anisotropic crystal, i.e. the tetragonal, orthorhombic, and rhombohedral phases of $BaTiO_3$, the polarization is described by,

$$P_i = (\varepsilon_{ij}-1)\,\varepsilon_0\,E_j\,. \qquad \text{(eqn 2.1)}$$

In the last equation, ε_{ij} is the dielectric tensor, and

$$X_{ij} = \varepsilon_{ij} - 1\,, \qquad \text{(eqn 2.2)}$$

X_{ij} is the susceptibility tensor. In the formation of the spontaneous polarization in $BaTiO_3$, some important concepts are involved such as, "Lorentz correction" and "Polarization catastrophe". These are the main factors that determine the ferroelectricity of the crystal (see for example [Ref. 4]) In this presentation, cubic symmetry was considered. Following Kittel [Ref. 4], the Lorentz correction correction is: the polarizing field acting on the crystal has to be different from the local field

$$\underline{E}_l = \underline{E} + (1/3\varepsilon_0)\underline{P}_s\,. \qquad \text{(eqn 2.3)}$$

In this equation, $\underline{E}_l$ is the local field, $\underline{E}$ is the external field, $\underline{P}_s$ is the spontaneous polarization and ε_0 is the dielectric permeability of space. The relation between polarizability and the dipole moment is given by

$$\underline{P} = b\underline{E}_l\,, \qquad \text{(eqn 2.4)}$$

where $\underline{P}$ is the dipole moment of an atomic or ionic species (assumed to be spherically symmetric) and b is the polarizability.

The polarizability is an microscopic parameter. The dielectric constant depends on the crystal symmetry which becomes a tensor for a non cubic cell. The spontaneous polarization is the sum of all the dipole moments per unit volume,

$$P_s = \sum N_j P_j = \sum N_j b_j E_l (j). \qquad \text{(eqn 2.5)}$$

In the last relation, N_j is the concentration and b_j is is the polarizability of atoms of type (j) and E_l (j) is the local field at the atoms sites (j). The next step is to find a relation between the dielectric constant and polarizabilities. Substituting the Equation 2.3 into 2.5 gives for cubic symmetry,

$$\underline{P}_s = (\sum N_j b_j)\{\underline{E} + (\underline{P}_s/3\ \varepsilon_0)\} . \qquad \text{(eqn 2.6)}$$

After some algebra, Equation 2.6 becomes

$$(\varepsilon - 1)/(\varepsilon + 2)\} = (1/3\ \varepsilon_0)\sum N_j b_j , \qquad \text{(eqn 2.7)}$$

the Clausius-Mossotti relation. At optical frequencies $n^2 = \varepsilon$ and Equation 2.7 then becomes

$$(n^2 - 1)/(n^2 + 2) = (1/3\ \varepsilon_0) \sum N_j b_j \text{ (electronic)} , \qquad \text{(eqn 2.8)}$$

where n is the index of refraction. Rearranging Equation 2.7, the dielectric constant takes the form

$$\varepsilon = \{1 + (2/3\ \varepsilon_0) \sum N_i b_i \}/ \{1-(1/3\ \varepsilon_0) \sum N_i b_i\} . \qquad \text{(eqn 2.9)}$$

In the last relation, b_i is the electronic plus ionic polarizability of (i) type ion and N_i is the concentration. The dielectric constant becomes infinite when the term in the denominator vanishes and leads to the "Polarization catastrophe". This means that $BaTiO_3$ has a finite polarization, even when there is no applied field. Indeed, the catastrophe occurs at the Curie point where the dielectric constant as a function of temperature has a peak, as is seen from Figure 2.5.

The polarization catastrophe occurs when

$$(1/3\,\varepsilon_0)\sum N_i b_i = 1 . \qquad \text{(eqn 2.10)}$$

In the original theory of Devonshire [Ref. 5], the ionic species were assumed to be spherically symmetric. Slater [Ref. 6] showed that Equation 2.10 can not be satisfied under the condition of spherical symmetry, so he introduced asymmetry of the ionic species.

The latest theories of $BaTiO_3$ unify Devonshire's theory and Slater's theory by taking into account the contributions by all ion motions to spontaneous polarization [Ref. 4]. As we see from Figure 2.4, Ba^{2+} and Ti^{4+} ions are displaced relative to the O^{2-} ions, where produces a dipole moment and then spontaneous polarization. The upper and lower oxygen ions may move downward slightly [Ref. 4].

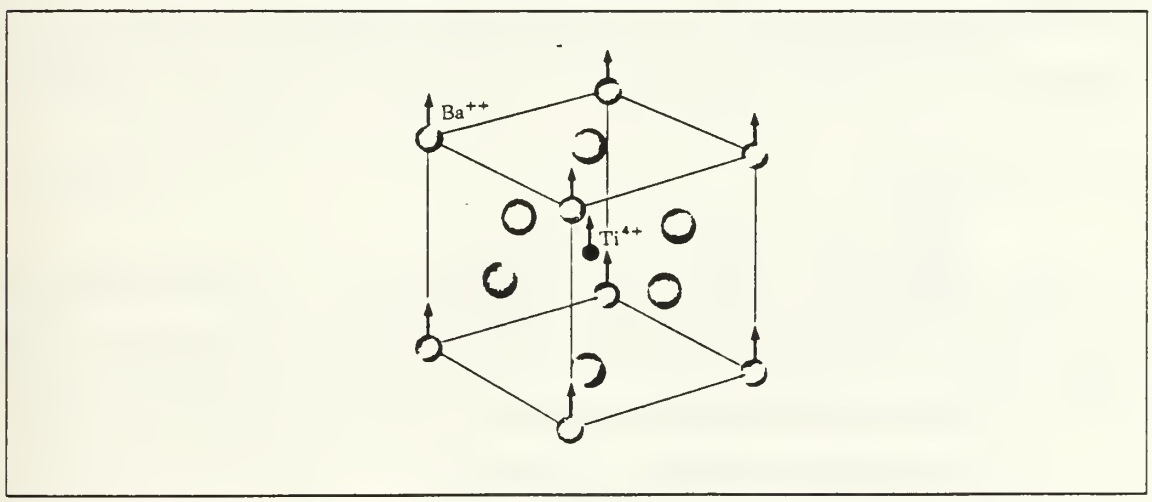

Figure 2.3 Ionic motions in $BaTiO_3$ [Ref.3].

The temperature dependence of spontaneous polarization was measured by Merz [Ref. 7], from hysteresis loops. This is illustrated in Figure 2.4.

2. **Dielectric constant of $BaTiO_3$**

As is seen from Figure 2.5, the tetragonal phase has two dielectric constants that are denoted by ε_a and ε_c . This is a result of the crystal symmetry and the tensor character of the dielectric constant.

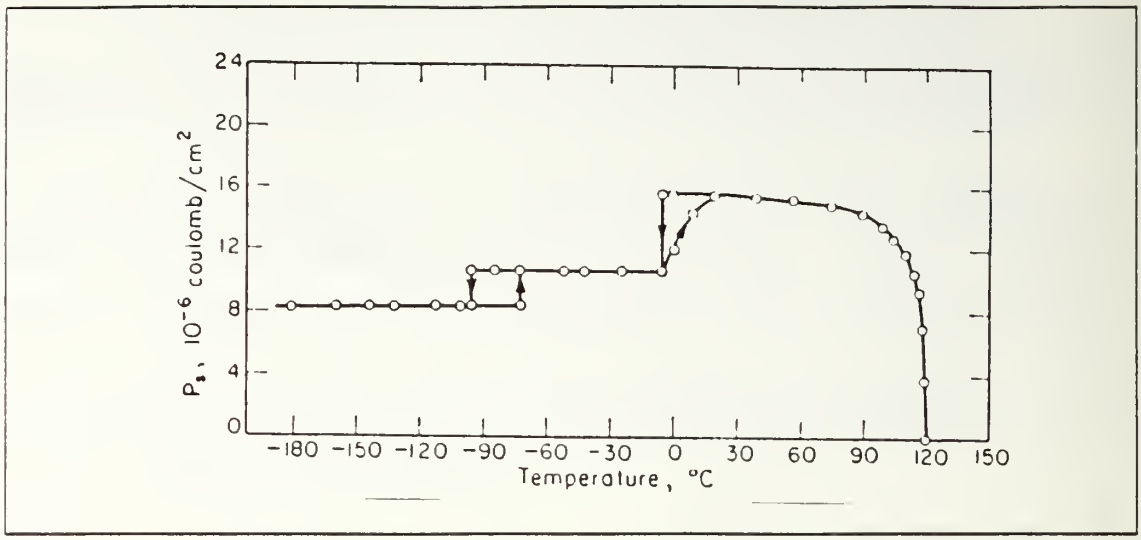

Figure 2.4 Temperature dependence of spontaneous polarization [Ref.6].

In the cubic phase, there is only one dielectric constant and above the Curie temperature, the dielectric constant obeys the Curie-Weiss law given by the relation

$$\varepsilon = \{ C/(T-T_c) \}. \qquad \text{(eqn 2.11)}$$

In the last relation, C is the Curie constant $\sim 10^5$ °K and T_c is the Curie temperature. As reported by Merz, dielectric constant measurements can be made precisely on single domain crystals. At low temperatures, the orthorhombic and rhombohedral phases of $BaTiO_3$ have two dielectric constants corresponding to the symmetry of the crystal.

3. **General ferroelectric properties of $BaTiO_3$**

This section summarizes the ferroelectric properties of $BaTiO_3$ 1) It has permanent spontaneous polarization below the Curie point and the direction changes with each phase. The magnitude of the spontaneous polarization changes with temperature as is seen from Figure 2.6. The spontaneous polarization demonstrates hysterises. 2) As we see from Figure 2.6, the magnitude of the spontaneous polarization decreases above 80°C. At the Curie point, spontaneous polarization vanishes. 3) Spontaneous polarization is in the direction of the c-axis of the crystal and it does not have components along the a-axis of the crystal. 4) The dielectric constant has a peak at the Curie temperature. 5) Above the Curie point the dielectric constant falls off and obeys the Curie-Weiss law. 6) At the Curie point a ferroelectric

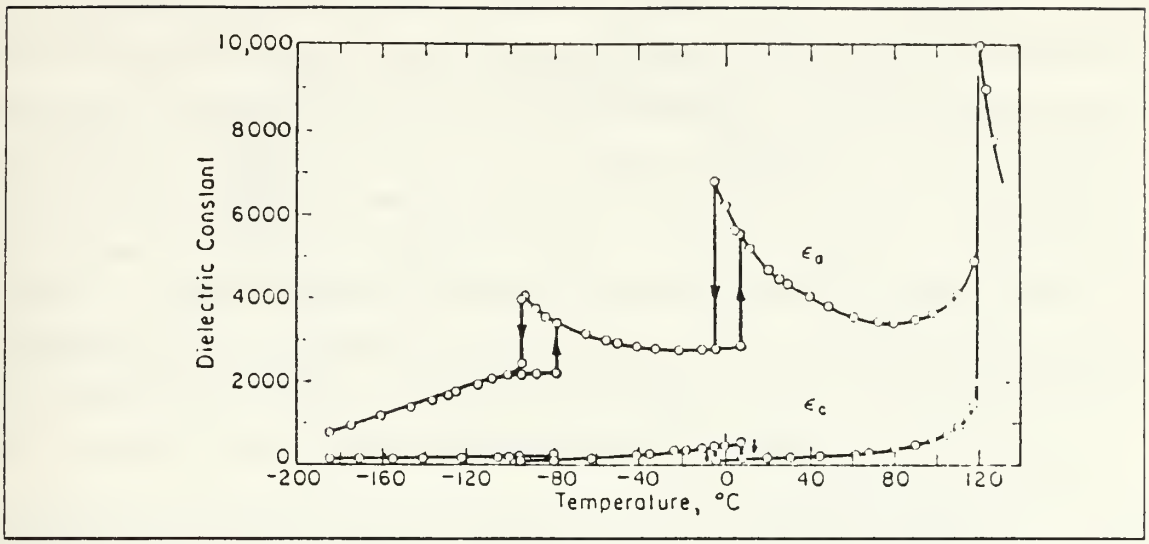

Figure 2.5 Dielectric constant of $BaTiO_3$ as a function of temperature T [Ref.2].

to paraelectric phase transition occurs. This is the so-called polarization catastrophe [Ref. 4].

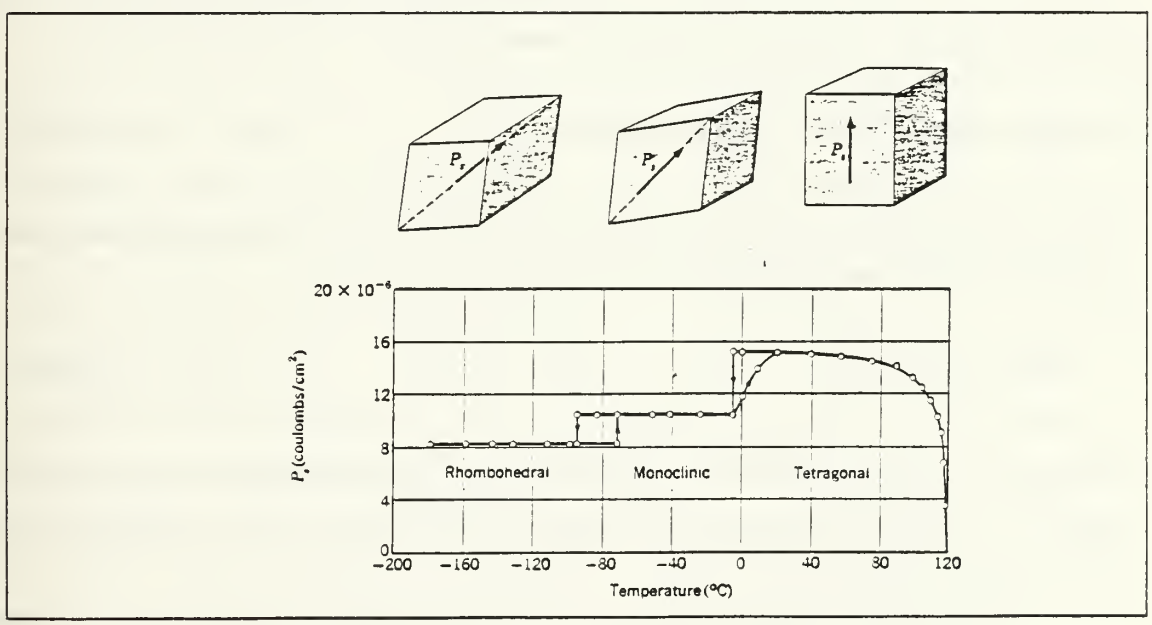

Figure 2.6 Spontaneous polarization vs temperature [Ref.6].

4. **The pyroelectric effect**

There is a direct relation between the spontaneous polarization (key component of ferroelectricty) and the pyroelectric effect. Lord Kelvin [Ref. 4] defined the pyroelectric effect as follows: "The pyroelectric effect is the change of spontaneous polarization due to temperature changes". So, it can be said that all ferroelectrics are pyroelectric, but the reverse is not true, because some pyroelectric crystals may not change their polarization direction, when the polarity of the field is reversed. The pyroelectric effect in $BaTiO_3$ has been studied by Chynoweth [Ref. 8]. When the crystal is illuminated , it causes a small change in temperature of the crystal which in turn causes the spontaneous polarization to change. In other words, radiation on the crystal causes first a temperature rise, then expansion of the crystal spacing, and finally a change in spontaneous polarization.

When electrodes are attached to the polar faces ($\perp$ to c-axis), the polarization produces a change in the charge on the electrodes, explained as follows: The change in the charge in time will cause the current to flow and can be detected by an external circuit. To develop a mathematical relationship consider a small temperature change dT that produces a change dP_s in P_s . If this temperature change occurs in a time dt, then the spontaneous polarization changes at the rate of (dP_s / dt), which is equivalent to a current density $\underline{J}_{py}$ detected by the external circuit,

$$\underline{J}_{py} = (dP_s / dt) = (dP_s/dT)\,(dT/dt). \qquad \text{(eqn 2.12)}$$

For a small temperature change, the term (dP_s /dT) can be taken as a constant and is called the "Pyroelectric coefficient" for a certain temperature.

$$p(T) = (dP_s/dT) \qquad \text{(eqn 2.13)}$$

where p(T) is the pyroelectric coefficient [Ref. 9]. This coefficient can be found for a specific temperature, from the slope of the P_s versus T curve, at that temperature, as is seen from Figure 2.7.

Since p(T) is approximately constant for a specific temperature, the current density $\underline{J}_{py}$ can be detected, if (dT/dt) is large enough. We know that the spontaneous polarization disappears at the Curie point and the crystal becomes paraelectric. Thus, the pyroelectric effect should not be observed above the Curie point, but has been

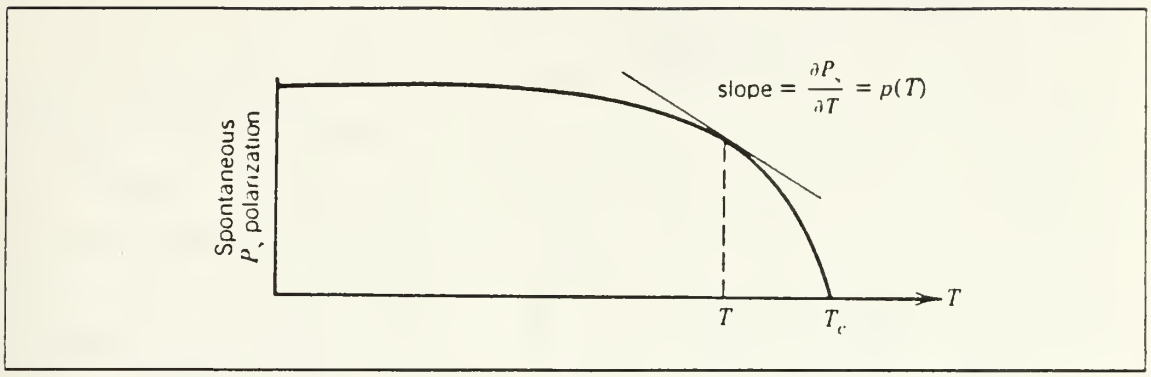

Figure 2.7 p(T) from P_s vs T [Ref.8].

observed by Chynoweth [Ref. 10] in $BaTiO_3$. He concluded that $BaTiO_3$ has surface space-charge layers and these charges produce a field through the interior of the crystal. Since temperatures above the Curie point were not used in this research, this is beyond the scope of our analysis. The derivation of the Equation 2.12 will be given in Section H.

C. BULK PHOTOVOLTAIC EFFECT

Chynoweth [Ref. 10] has reported observing the photovoltaic effect in $BaTiO_3$ above the Curie temperature. It has been interpreted as a result of a space-charge field due to surface charge layers. This argument led Chen to explain photorefraction in electrooptic crystals incorrectly. [Ref. 1]. Glass [Ref. 11] explained the microscopic origin of the photovoltaic effect and its contribution to photorefraction. Later, Gower [Ref. 12] observed the bulk photovoltaic effect in $BaTiO_3$ at room temperatures. Summarizing the previous works, the observed properties of bulk photovoltaic effect (BPVE) in $BaTiO_3$ are : 1) Brody [Ref. 13] observed that the photovoltage ($\sim$ 100-200V) is linearly dependent on the spontaneous polarization and independent of laser intensity. 2) Brody [Ref. 13] observed that the photovoltage vanishes above the Curie temperature (recall spontaneous polarization vanishes above 118°C). 3) Koch et al. [Ref. 14] have observed that the short circuit photovoltaic current (SCPVC) vanishes at temperatures above the Curie point, and the SCPVC is linearly dependent on intensity. 4) the BPVE exists even in the absence of an external electric field in the pyroelectric crystals. Thermal excitation does not produce the BPVE.

Now with the help of these observations, we can compare the BPVE with conventional photovoltaic effects. In general there are two types of photovoltaic

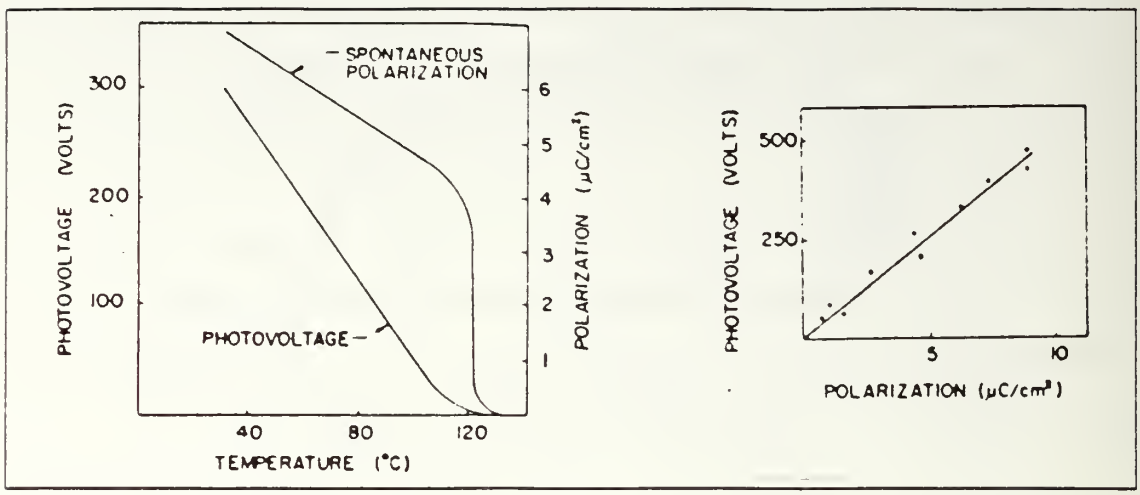

Figure 2.8 Photovoltage vs temperature [Ref.13].

effects. The first one is known as the Dember or photon drag effect and appears when incident radiation on the surface is strongly absorbed by the semiconductor. A potential difference developes in the direction of the radition because of a difference between electron and hole mobilities [Ref. 15].

The second type of photovoltaic effect results from homogeneous absorption in the crystal containing macroscopic inhomogeneities, as in semiconductor p-n junctions. Differences in the Fermi levels bend the conduction and valence bands.

The photovoltaic effect in $BaTiO_3$ occurs only along the c-axis, which is the spontaneous polarization direction. In our experimental geometry, the incident beam direction was perpendicular to the c-axis. Thus, the possibility of the Dember effect was ruled out. When the electrodes were attached to the polar faces, which were perpendicular to the c-axis, the photo-voltage across the polar faces was around 10V. This number is too big to be due to a difference in Fermi levels of a p-n junction mechanism (around 1V). A possible explanation might be a number of p-n junctions connected serially to give 10V. The macroscopic homogeneity of $BaTiO_3$ does not allow us to construct a model of this kind; so this possibilty is ruled out.

Thus, it was seen that there is no direct anology between BPVE and the conventional photovoltaic effects. So, what is the BPVE and what kind of mechanism causes this effect ? In order to answer these questions, we will follow Glass et al. [Ref. 16] for the intrinsic (pure) crystal, and then for the extrinsic (impure) case.

INTRINSIC BPVE : Glass et al. [Ref. 16] considered a one dimensional polar structure, in which a unit cell contains an anion O and a cation B. In $BaTiO_3$ anions are O^{2-} ions and cations are Ti^{4+} ions. The top of the valence band contains oxygen 2p states and the conduction band contains Ti 3d states. BPVE in pure (no impurity) pyroelectrics occurs as follows: optical transitions are delocalized transitions, provided that there is an electron-phonon coupling in the polar crystal. As is shown in Figure 2.9, GS represents the ground state of a one dimensional polar structure. Consider an optically stimulated excitation that causes a transfer of charge from an anion to the nearest cation. Glass et al. [Ref. 16] assumed that a charge ε ($<<$ electronic charge) per unit cell distributed over the entire chain was transferred in each unit cell. In the one dimensional argument, charge transfer occurs only along the c axis. Figure 2.9b and c, shows the charge distribution after excitation in the Frank-Condon state (FCS) and relaxed state (RES). The Franck-Condon principle says that when an charge is excited optically, the nuclei of the ions may be considered to remain at rest during this process. In other words, an optical excitation occurs in a very short time compared with the period of corresponding lattice vibrations. In Figure 2.9c, the ionic shift has been greatly exaggerated.

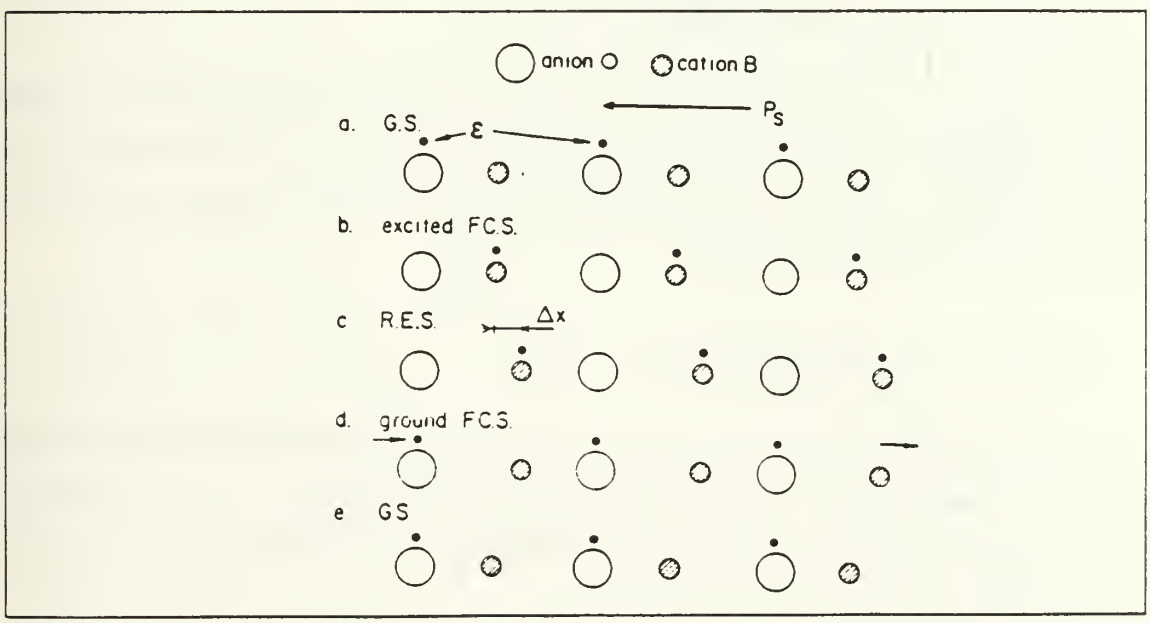

Figure 2.9 Charge distributions of intrinsic BPVE [Ref.16].

Figure 2.9 shows that charge moves continuously to the right but in general, the probability of charge transfer to the right and the left will be different during excitation and recombination. This will result in a steady state photo current. This model looks like a microscopic shift register, in which charge ε is transferred from one unit cell to the next by ionic relaxation in a random manner. Glass et al. [Ref. 16] have performed calculations based on these ideas.

EXTRINSIC BPVE : This case is similar to the previous one, except there are impurities in the crystal. The type of impurities in $BaTiO_3$ will be mentioned in the next section. Baltz et al. [Ref. 17] took up this case, in order to a derive short circuit photovoltaic current (SCPVC) quantum mechanically, which was originally given by Glass. For convenience, we will follow their arguments to summarize extrinsic BPVE. They have considered a one dimensional model of a photo-excited carrier in a nonsymmetric potential $V(x) \neq V(-x)$ which simulates the existence of an acentric impurity. In Glass's model, the SCPVC is due to electronic transitions from a localized ground state $|0>$ into the delocalized states $|+>$ and $|->$, in which the photo-excited carrier moves along the $+c$ and $-c$ directions. Since the potential is asymmetric, the photoionization probabilities p_+ and p_- are different. This results in currents J_+ in the $+c$ direction and J_- in the $-c$ directions subject to

$$(dJ/dt)+(1/\tau)J = (e\alpha I/h\nu)vp . \qquad \text{(eqn 2.14)}$$

This equation is valid for J_+ and J_-. Here, τ stands for the life time of the carrier which depends on the recombination and collision rates, I is the intensity of the incoming beam, α is the absortion coefficient and v is the carrier velocity. In the steady state, the net SCPVC is given by

$$J_{ph} = J_+ - J_- = (\alpha\, Ie/h\nu)(l_+\, p_+ - l_-\, p_-). \qquad \text{(eqn 2.15)}$$

In this equation, $l_+ = v_+\, \tau_+$, $l_- = v_-\, \tau_-$ and l_+ and l_- are the mean free path lengths of the excited carriers. In the case of thermal excitation, $J_{ph} = 0$, because the probabilities of excitation and recombination in the directions $+c$ and $-c$ of the crysatal are the same,

$$p_+ \text{ (thermal)} = p_- \text{ (thermal)} = \exp(-E/kT). \qquad \text{(eqn 2.16)}$$

Here, k is Boltzman's constant and E is the energy of the particular state. In the literature, J_{ph} usually is given by this form [Ref. 11]

$$J_{ph} = \kappa(\nu)\alpha(\nu)I. \qquad \text{(eqn 2.17)}$$

In the last equation, κ is the anisotropy constant which depends on the frequency ν and the nature of the absorption centre. It represents the difference in probabilities times the mean free path length charge moving in the + and - c axis direction. It is independent of the crystal geometry, the electrode configuration, and the impurity concentration. Glass's model, predicts the mean displacement of the photo carriers per excitation, which is restricted to the lattice constant.

D. SEMICONDUCTOR PROPERTIES OF $BATIO_3$

$BaTiO_3$ has a very small conductivity. Gower [Ref. 12] has found a conductivity of ~ $0.8*10^{-10}$ I (ohm cm)$^{-1}$, where I is the laser intensity. The energy band gap is ~ 3eV. These numbers show that $BaTiO_3$ is a semiconductor. The semiconducting properties of $BaTiO_3$ are thought to be important in the origin of photorefraction. As has been reported by Klein et al. [Ref. 18] and Feinberg et al. [Ref. 19], impurities determine the semiconductor properties of $BaTiO_3$. At the present time, however, little is known about the impurities that are responsible for photorefraction. We will summarize the experimental results of Klein and Feinberg about the impurity properties, Before geting into the details, it will be useful to enumerate some basic definitions for semiconductors. Donors are the type of impurities which can give up electrons. In this process, since the electrons still stay in the crystal, the entire crystal stays neutral. Acceptors, can receive electrons from the valence band, in order to complete the covalent bonds between neighboring atoms. In this case, a vacancy or

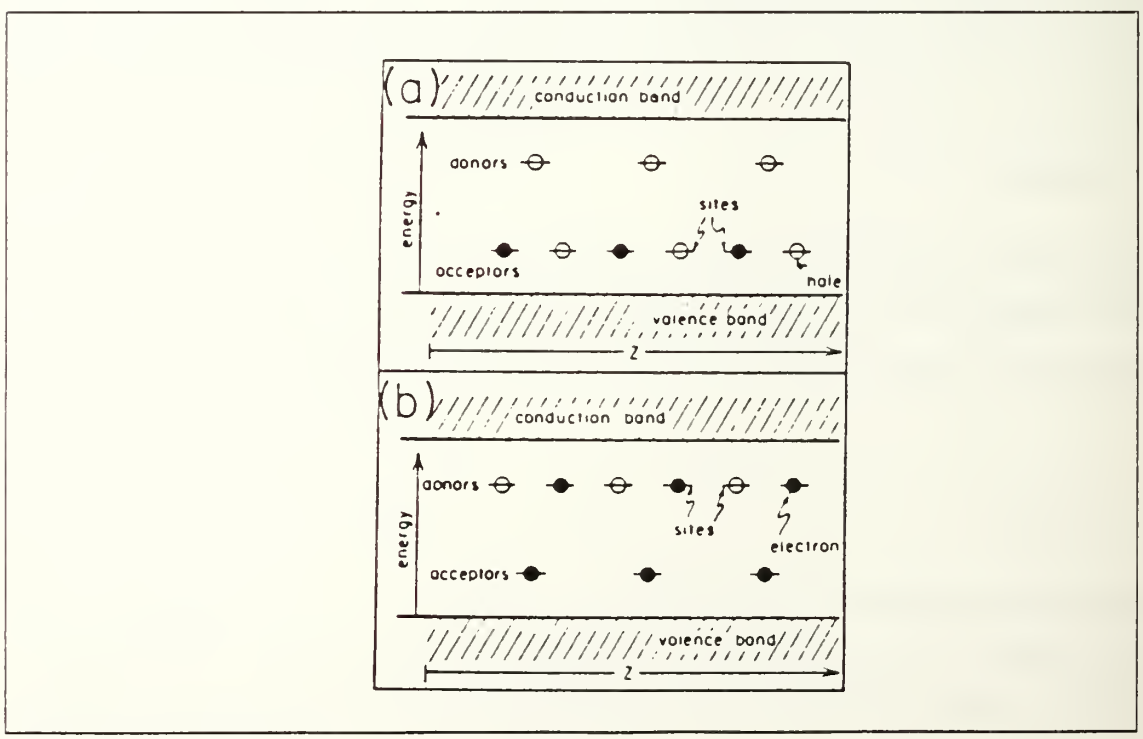

Figure 2.10 Donors-Acceptors in a ferroelectric semiconductor [Ref.19].

(a) Majority carriers are holes. (b) Majority carriers are electrons.

hole is created for each electron removed from the valence band. A hole acts like a positive charge under an applied field. The mobility is the magnitude of the drift velocity per unit electric field and is positive for electrons and holes, even though their drift velocity is opposite. The hole mobility is smaller than the electron mobility [Ref. 4]. In a P type crystal, acceptors are dominant which means holes are the majority carriers, and the electrons are minority carriers, this is shown in Figure 2.10a. In an N type crystal, donors are dominant, so the electrons are majority carriers and the holes are minority carriers. This can be seen from Figure 2.10b.

Klein et al. [Ref. 18] reported three major groups of impurities in $BaTiO_3$: 1) Ca and Sr are in the same group with Ba. They are always together with Ba in nature and it is difficult to separate them. They assumed that Ba does not play an important role in photorefraction. Therefore, Ca and Sr do not introduce any energy levels in the energy band gap of $BaTiO_3$. 2) Al and Si exist in the crystal because of the furnace walls and heating elements used during the crystal growth process. Since they have only one stable valence state namely Al^{3+} and Si^{4+} , they can not be involved in the intervalence charge transfer. The existence of transition metals in many oxide crystal is unavoidable because of their abundance in nature, and is important in photorefraction. The first six transition metals are Cr, Mn, Fe, Co, Ni and Cu. They are more than likely to be present in $BaTiO_3$. Klein et al. [Ref. 18], have done absorption coefficient measurements, electron paramagnetic resonance (EPR), beam coupling and spark source emission spectroscopy (SIMS) experiments. These experiments showed that Fe is the impurity responsible for photorefraction, and the holes are the majority carriers. They concluded that the filled acceptors are Fe^{3+} and the empty acceptors are Fe^{2+} ions. The ion concentration were given as

$N = \{Fe^{2+}\} \sim (2\text{-}9)*10^{16}\ cm^{-3}$,

and

$N^{+} = \{Fe^{3+}\} \sim (2\text{-}8)*10^{18}\ cm^{-3}$.

According to Klein et al., the Fe^{2+} / Fe^{3+} ratio governs the photorefraction properties of $BaTiO_3$. We see from Figure 2.11 that the relative contribution of holes and electrons to photorefraction depends on the Fe^{+2}/Fe^{+3} ratio.

An alternative interpretation was given by Feinberg et al. [Ref. 19]. They were able to alter the photorefractive properties of a nominally pure single crystal of $BaTiO_3$ by treating the crystal at 650°C in oxygen at different partial pressures. This treatment caused the effective density of photorefractive charge carriers to change in the crystal

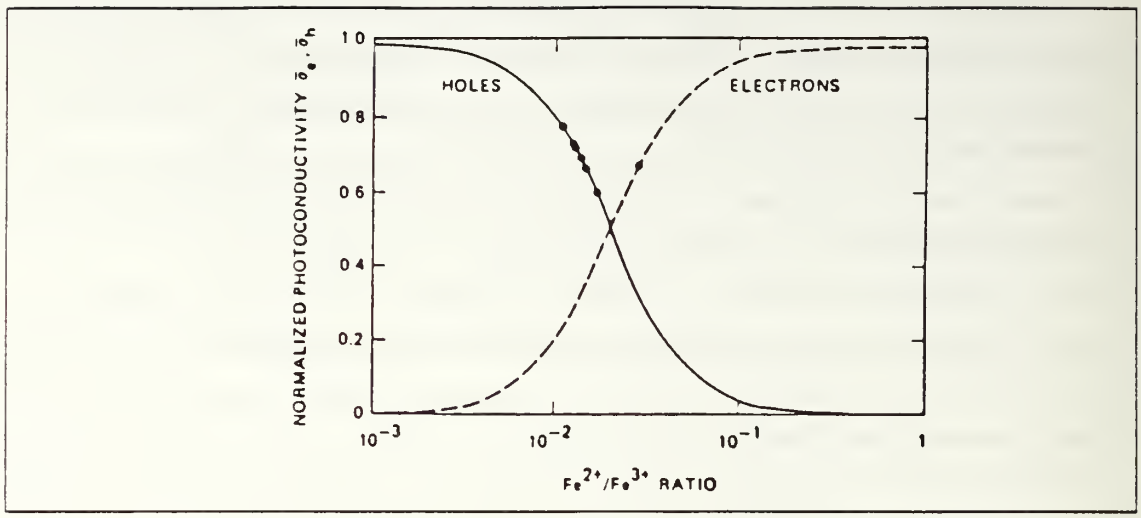

Figure 2.11 Relative contribution of electrons and holes to the photoconductivity [Ref.18].

and could convert a dead (inactive in photorefraction) crystal into a live (active) one. Reduction (treatment at low temperature) decreases the Curie temperature of the crystal and also decreases the energy band gap, implying that oxygen vacancies were added to the bulk crystal. Negative photorefractive charge donors are associated with these oxygen vacancies, depending on whether the partial pressure of oxygen was greater than or less than 0.5 atm during the treatment. Either holes or electrons may be the majority carriers. According to Feinberg et al. [Ref. 19] electron and hole contributions to the photoconductivity were found to vary with the density of oxygen defects (vacancies) introduced into the crystal during the treatment. As we see from Figure 2.12, the crystal switches from N type to P type at an oxygen pressure of ~ 0.5 atm in which the effective density N_{pr} of the photorefractive charges is minimum. They reported that, in their samples, the effective density of photorefractive charge carriers was

$$N_{pr} \sim (0.3\text{-}6.2)*10^{16}\ cm^{-3}\ .$$

Between these two studies, there is a major discrepancy. For instance, Klein et al. [Ref. 18] assumed that the oxygen vacancy can trap one or two electrons, leaving donor levels in the $BaTiO_3$ energy band gap. But, for two reasons, these levels can not participate in the photorefraction: 1) The donor levels, which are occupied by oxygen vacancies and are relatively shallow, can be thermally ionized at room temperature. 2) According to Klein et al.'s beam-coupling experiments, the holes are majority carriers

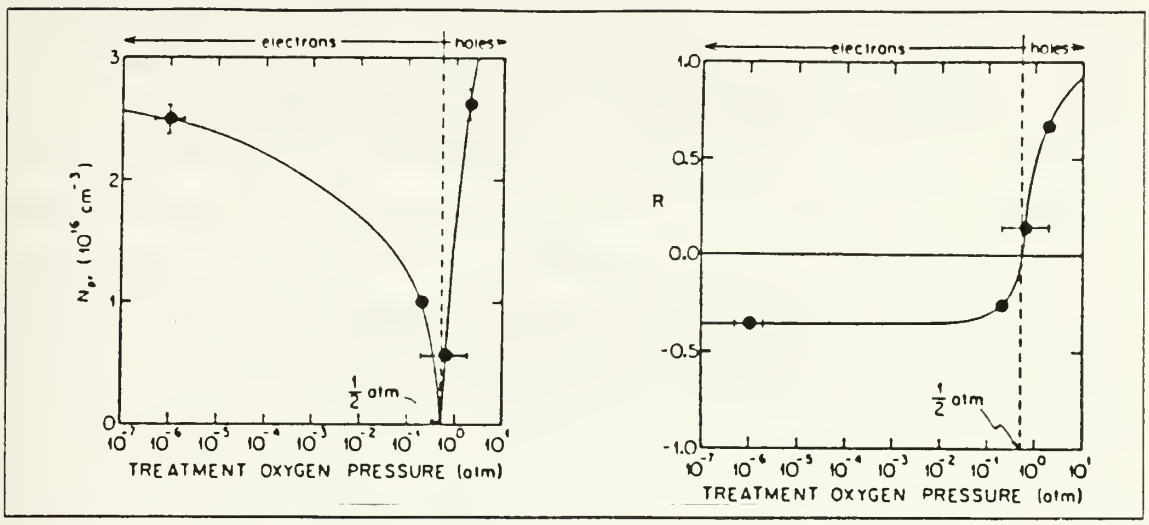

Figure 2.12 Oxygen vacancies as photorefractive centres [Ref.19].

(a) Density of photorefractive carriers vs oxygen pressure. (b) Relative contribution (R) of holes and electrons to photorefraction.

in contradiction to the donor character of the oxygen vacancies. However, according to Feinberg et al. oxidation and reduction treatments only change the density of oxygen vacancies (donors) and not barium vacancies (acceptors). On the other hand, if Fe is an active photorefractive impurity, then Fe^{2+} ions are donors and Fe^{3+} ions are acceptors, and the oxidation-reduction treatments would have changed the densities of both donor and acceptor levels. Feinberg et al. [Ref. 19], suggested that annealing experiments should be performed at very low oxygen pressure. According to Feinberg et al. (oxygen vacancy picture), this treatment would increase the density of donors (oxygen vacancies) without changing the density of acceptors (barium vacancies) and would create an effective photorefractive charge density. However, according to Klein et al. (Fe picture), this treatment would cause all the acceptors to be converted into donors, resulting in no effective photorefractive charge density.

ENERGY LEVELS OF TETRAGONAL $BATIO_3$:

In Figure 2.13, CB is the conduction band and VB is the valence band. and O_h and C_{4v} stand for cubic and tetragonal $BaTiO_3$. The top of the valence band is composed of oxygen 2p states and the conduction band is Ti 3d states for the cubic and tetragonal symmetries. On the other hand, the energy levels of the Ba ion do not play an important role in photorefraction (according to Klein et al.,) and are not illustrated. In

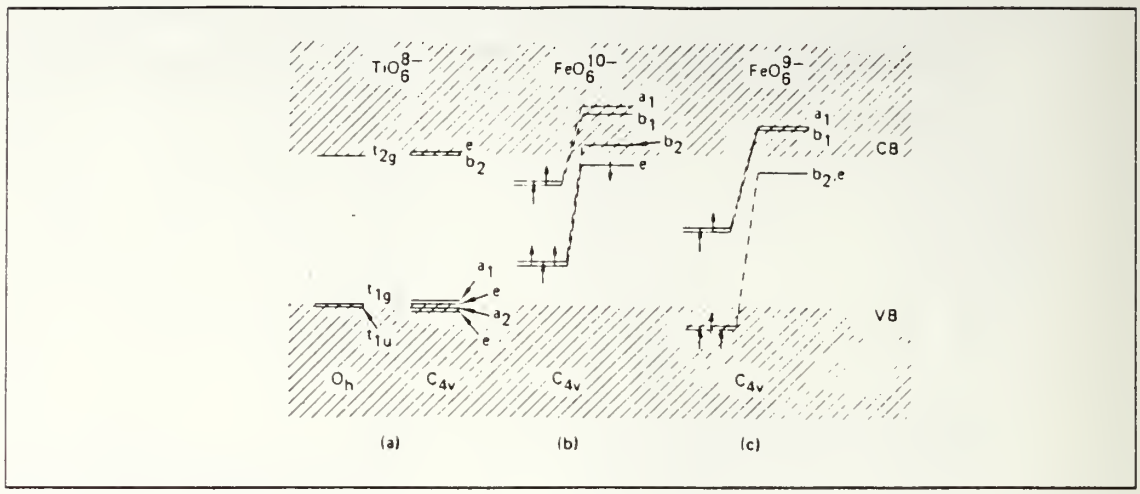

Figure 2.13 Energy levels of $B^{n+}\ O_6^{\ -12+n}$ clusters in $BaTiO_3$ [Ref.18].

the cubic symmetry, the valence band edge decomposes into states labeled t_{1g} and t_{1u} and the bottom of the conduction band is labeled as t_{2g}, as is shown in Figure 2.13a. A phase transition from cubic to tetragonal symmetry results in split and shifted energy levels (see Figure 2.13a). Fe^{2+} ($FeO_6^{\ 10-}$) and Fe^{3+} ($FeO_6^{\ 9-}$) have a complex energy level structure in $BaTiO_3$. However, Fe^{2+} and Fe^{3+} complexes do have localized states in the energy band gap. The spin-up (↑) states (generally occupied) are donors and spin-down (↓) states (generally empty) are acceptors, as is seen from Figure 2.13 b and c. Thus, with this picture heteronuclear intervalence transitions involving 2p→ Fe 3d and Fe 3d→ Ti 3d transitions with photon energies less than the energy band gap are possible.

Hellwarth et al. [Ref. 20] showed that electrons and holes can exist simultaneously under the illumination of the crystal.

E. CHARGE TRANSPORT IN $BATIO_3$

Charge transport may be caused by drift, diffusion and the bulk photovoltaic effect (BPVE) mechanisms. Currently, there are two models in which these mechanisms are used in different ways to explain photorefraction.

BAND MODEL: This model has been proposed by Kukhtarev et al. [Ref. 2] and Young et al. [Ref. 21]. In the previous section, the simultaneous existence of electrons and holes has been mentioned. So, charge transport is possible by both electrons and holes. The band model however is based on only electron transport or only hole

transport. It does not handle electron and hole transport simultaneously. According to the band model, electron transport is a three step process: 1) Photoionization of an electron from filled state (donor) to the conduction band. 2) Migration of the photoexcited electrons to dark regions in the crystal can be caused by drift and diffusion through the conduction band. 3) Finally, recombination at an empty state (ionized donor). Hole transport is also a three step process, in this case X^+ is an acceptor or filled state. The three steps are: 1) Photoionization of a hole from an acceptor X^+ to the valence band. 2) Migration of photoexcited hole to dark regions by diffusion and drift, through the valence band. 3) Recombination at an ionized acceptor or empty trap site X. Figure 2.14 summarizes these ideas.

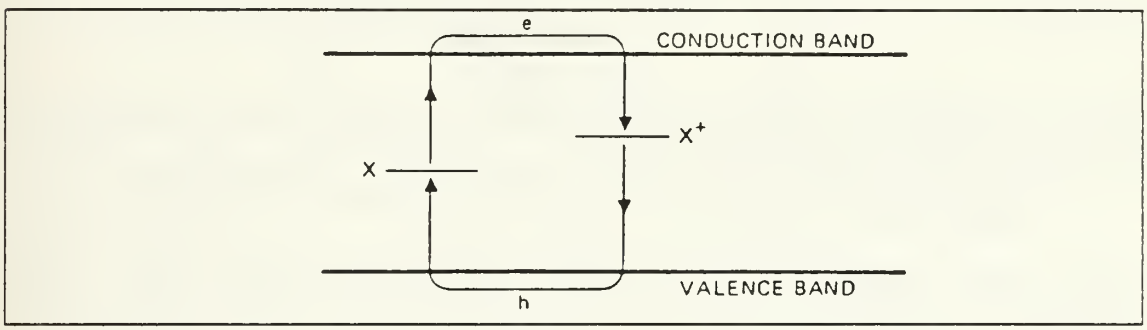

Figure 2.14 Band model of charge transport in $BaTiO_3$ [Ref.18].

According to Klein et al. X corresponds to Fe^{2+} and X^+ corresponds to Fe^{3+} . On the other hand, according to Feinberg et al. X corresponds to oxygen vacancies and X^+ corresponds to barium vacancies. If electrons diffuse away from the illuminated region, the resulting space charge field will be directed to the dark regions, as is seen from Figure 2.15a. If holes diffuse away from the illuminated region, then the space charge field will be directed to the illuminated regions.

As we see from Figure 2.15a and 2.15b, the sign of the space-charge field is opposite for the two charge carriers.

HOPPING MODEL: This model has been proposed by Feinberg et al. [Ref. 22]. According to this model, carriers move by hopping from a filled state to a neighbor empty state (trap). This model assumes single hops (photo assisted tunneling) between filled and empty sites. The semiconductor can conduct in the impurity band (the energy levels of the impurities in the energy band gap) by electrons hopping from a filled donor to an ionized donor. Impurity band conduction sets in at lower donor

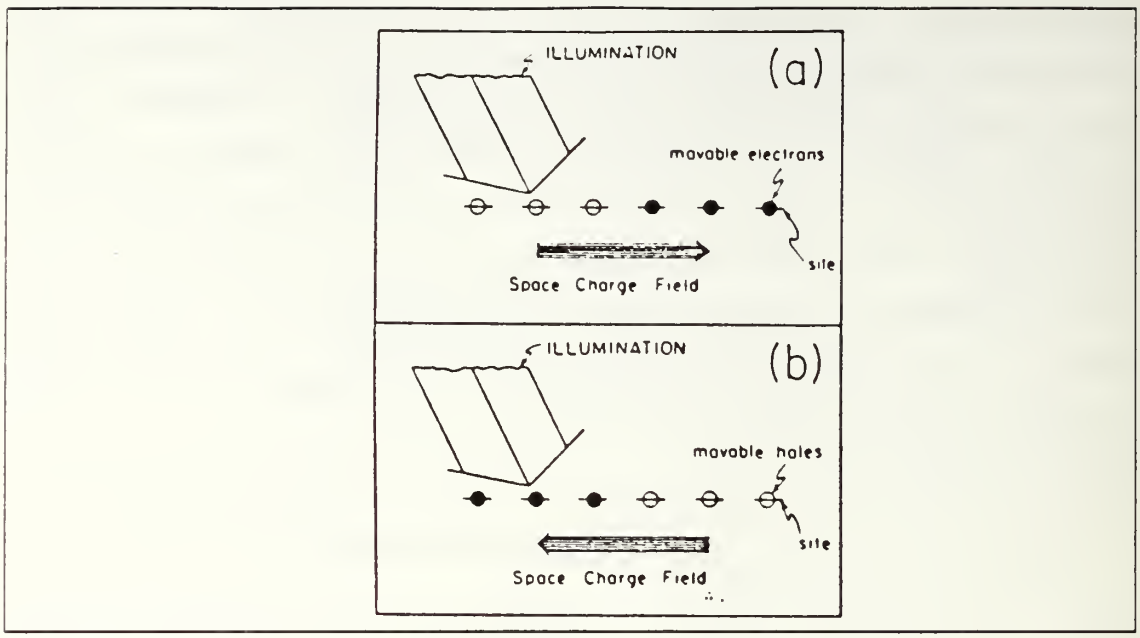

Figure 2.15 Redistribution of charges under illumination [Ref.19].

density levels if there are acceptors present to ionize some of the donors. Under illumination, electrons from donors will prefer to hop to an ionized (empty) donor, rather than to a filled donor atom.

These two models predict the same results as long as the electron (hole) recombination time is short compared to any optical excitation, and the relative charge modulation is small. The band transport model has been used widely in the literature. This model will be followed from now on.

DRIFT: Photoexcited carriers, electrons in the conduction band or holes in the valence band, can move freely under an external electric field. Carriers migrate out of the illuminated region, until they are trapped by empty traps near the beam periphery. An external field produces drift of photoexcited carriers through the band. Positive and negative charge separation during drift gives rise to a space-charge field and this in turn acts as feedback to redistribute the charges. The drift current density J_{dr} is given by

$$J_{dr} = e\mu_e nE + e\mu_h pE . \qquad \text{(eqn 2.18)}$$

In the last equation, μ_e , μ_h are electron and hole mobilities; n, p are electron and hole densities. $E = E_{ext} + E_{sc}$, where E_{ext} is the external field and E_{sc} is the photoinduced space-charge field (vector signs will be dropped from now on, considering the c-axis direction). Drift charge transport is caused by photoconductivity σ ,

$$J_{dr} = \sigma E , \quad \sigma = e\mu_e n + e\mu_h p. \qquad \text{(eqn 2.19)}$$

The charge transport length in this process is, $L_e = \mu \tau E$, where τ is lifetime of the carrier.

DIFFUSION: Due to thermal motion of the excited carriers, charge will diffuse depending on the gradient of the carrier concentration.

$$J_{dif} = eD_e (dn/dz) - eD_h (dp/dz) \qquad \text{(eqn 2.20)}$$

In this equation, $D_{e'h} = \mu_{e'h} (kT/e)$ are the Einstein diffusion coefficients for electrons and holes. Photoexcited charges travel a characteristic distance which is called, the diffusion length,

$$L_d = (D_{e'h} \tau)^{1/2} . \qquad \text{(eqn 2.21)}$$

In the steady state, the space-charge field will saturate, satisfying the relation

$$J_{dr} + J_{dif} = 0 . \qquad \text{(eqn 2.22)}$$

This can be written explicitly in the form

$$en(z)\mu (z) E(z) + eD(dn/dz) = 0 . \qquad \text{(eqn 2.23)}$$

With uniform illumination and zero external field ($E_{ext} = 0$; $E = E_{sc}$) and with the charge density along the z axis(c-axis) given by $n(z) = \sin Kz$, where K is a wave number, the space-charge field is

$$E_{sc} = (kT/e)(K \cos Kz/\sin Kz). \qquad \text{(eqn 2.24)}$$

The last equation alone can not cause photorefraction, because BPVE was not taken into consideration.

BPVE: As explained before, this effect was described by the photocurrent density $J_{ph} = \kappa \alpha I$. Now, the general charge transport can be written in terms of a total current density J as

$$J(z,t) = \sigma E(z,t) + eD\{dn(z,t)/dt\} + \kappa \alpha I(z,t). \qquad \text{(eqn 2.25)}$$

In this equation, the first term is due to drift, the second term is due to diffusion and last term is due to BPVE. Depending on the magnitude of these terms, one of them can dominate the others. In this equation, $n(z,t) = n_d + n_l (z,t)$, where n_d is the thermally excited carrier concentration in the dark and $n_l (z,t)$ the excited carrier concentration in the illumination. First Young et al. [Ref. 21] and later Kukhtarev et al. [Ref. 2] have discussed the principles of photorefraction theory. The common concept of these studies was based on two crucial points: 1) A dynamic theory has to be included in the model in order to explain the oscillatory behavior. 2) The effect of the space-charge field feedback on the redistribution of electrons has to be considered to predict the saturation of the field. This can be done by including the dark conductivity in the model. According to Kukhtarev et al. electrons are the majority carriers and they will be excited from trap centers (filled states) to the conduction band when the crystal is illuminated. Electrons in the conduction band will migrate out of the illuminated regions, under drift, diffusion or BPVE, until they are traped by empty states around the beam periphery. The rate of electron excitation into the conduction band is $\{sI(z,t) + \beta\} N_d$, where s is the cross section for photoionization, β the thermal excitation rate of electrons, N_d the concentration of filled states (donors). The recombination (traping) rate is $\gamma_r n N_a$, where γ_r is the recombination constant, n is the concentration of electrons in the conduction band, N_a is the concentration of empty states (trapping centres or ionized donors). Photoionization of the donors will cause charge transport and recombination. Then, the total change of n will be determined by the continuity and rate equations. The continuity equation is given by

$$dn(z,t)/dt = dN_a (z,t)/dt - (1/e)(dJ(z,t)/dz). \qquad \text{(eqn 2.26)}$$

The rate equation is given by

$$dN_a(z,t)/dt = (sI(z,t)+\beta)(N(z,t)-N_a(z,t))-\gamma_r\, n(z,t)N_a(z,t). \qquad \text{(eqn 2.27)}$$

In the last equation, $N = N_a + N_d$ is the total concentration of dopants, and it is assumed that only a small part of the donors will be ionized. The excited carrier lifetime is $\tau = \{1/(\gamma_r N_a)\}$ and is assumed to be independent of n. In thermal equilibrium, the thermal excitation rate is equal to the recombination rate $\beta N = n_d/\tau$. If these relations are invoked in the rate equation, then it takes the form,

$$dN_a(z,t)/dt = g(z)-(n(z,t)-n_d)/\tau \qquad \text{(eqn 2.28)}$$

In the last equation, g(z) is the generation rate, which is assumed to be proportional to the light intensity I. The generation rate is usually given by

$$g(z) = (\alpha\, Q)/(h\nu)I(z). \qquad \text{(eqn 2.29)}$$

In the last equation, Q is the quantum efficiency, h is Planck's constant and α is the absorption coefficient. Inserting these relations in the continuity equation gives

$$dn(z,t)/dt = g(z)-\{(n(z,t)-n_d)/\tau\}-(1/e)\{\partial\, J(z,t)/\partial\, z\}. \qquad \text{(eqn 2.30)}$$

In the last equation, the first term represents the generation of photocarriers, per unit volume per second due to the photoexcitation process. The second term represents the number of carriers trapped per second per unit volume due to the recombination process. The last term stands for carriers leaving a unit volume per second, due to a current density. At any point and time, the accumulation rate of the space-charge density is given by the continuity equation in one dimension,

$$\partial\, \rho_{sc}(z,t)/\partial\, t = -\partial\, J(z,t)/\partial\, z. \qquad \text{(eqn 2.31)}$$

Combining the last relation with Poisson's equation ($\nabla \cdot \underline{E}_{sc} = \rho_{sc}/\varepsilon$) gives

$$\partial\, E_{sc}/\partial\, z = -(1/\varepsilon)\int_0^t (\partial\, J(z,t)/\partial\, z)dt + F'(t). \qquad \text{(eqn 2.32)}$$

Integration of the last equation, with respect to z, gives the photo-induced space-charge field,

$$E_{sc}(z,t) = -(1/\varepsilon)\int_0^t J(z,t)dt + F(t). \qquad \text{(eqn 2.33)}$$

In the last equation, F(t) can be determined from the boundary conditions, as in the following case. A constant voltage source, of voltage V, is applied across the crystal, so that $E_{ext} = V/L$, where L is the difference between electrodes. Integration of the total field, $E(z,t) = V/L + E_{sc}$, must still give V,

$$\int_0^1 E(z,t)dz = V, \qquad \text{(eqn 2.34)}$$

so that

$$\int_0^1 E_{sc}(z,t)dz = 0. \qquad \text{(eqn 2.35)}$$

This relation is true, even in the short circuit configuration.

Recently, Young et al. [Ref. 23] found expressions for E_{sc}, by solving Equation 2.31 and 2.33. Their model does not include the contribution of holes in the general transport equation. On the other hand Valley [Ref. 24] almost found a complete expression for E_{sc}. This model does not include BPVE, so that it can not explain the steady-state condition. A complete dynamic theory has to be able to solve the continuity, rate, general transport, Poisson's and wave equations, simultaneously. Also the general transport equation has to include diffusion, drift , BPVE processes and the contribution of holes.

F. ELECTROOPTIC EFFECT

The electrooptic effect is the change of the index of refraction, due to an external field or space charge field. We know that $BaTiO_3$ is a ferroelectric crystal with a phase transition at the Curie point. Between 118°C and 5°C, it has tetrogonal symmetry which is noncentrosymmetric with point group 4mm. In this phase the linear (Pockel) electrooptic effect is important. Above the Curie point the crystal becomes centrosymmetric with point group m3m and is cubic. In this phase the Pockel effect disappears. So, it is clear that symmetry plays an important role in the electrooptic effect.

Next consider the electromagnetic wave propagation in the crystal. The media through which the electromagnetic wave propagates, determines the characteristic behavior of the wave. The media we are dealing with in this thesis is a macroscopically homogeneous, anisotropic and nonlinear crystal.

Electromagnetic wave propagation in the crystal is completely described by the index ellipsoid or indicatrix [Ref. 25]. In general, the indicatrix is given by

$$\{X^2 / n_1 2\} + \{Y^2 / n_2 2\} + \{Z^2 / n_3 2\} = 1 . \qquad \text{(eqn 2.36)}$$

In the last equation, $X = D_x / (\varepsilon_0 E_x D_x)^{1/2}$, $Y = D_y / (\varepsilon_0 E_y D_y)^{1/2}$, $Z = D_z / (\varepsilon_0 E_z D_z)^{1/2}$, where D_x , D_y and D_z are the components of the displacement vector, and n_1 , n_2 and n_3 are the refraction indices along the principal axes of the ellipsoid. In the presence of the electric field in the crystal, the indicatrix equation is modified

$$a_{11} X^2 + a_{22} Y^2 + a_{33} Z^2 + 2a_{23} YZ + 2a_{31} ZX + 2a_{12} XY = 1$$
. (eqn 2.37)

In this equation, a_{ik} are the polarization constants. The linear change in the polarization constants due to a field is given by

$$a_{ik} - \{1/ n_i n_k\}\delta_{ik} = \sum_l r_{ikl} E_l . \qquad \text{(eqn 2.38)}$$

In the last equation, the summation includes $l = 1$ to $l = 3$. The δ_{ik} is the Kroneker delta function, r_{ikl} is the electrooptic tensor and n_i is the diagonal element of the index of refraction tensor. Following Johnston [Ref. 26], the index of refraction change along the c-axis is

$$\delta (n_3) = \{n_3 3 \, r_{33} \, \delta P_s\} / \{2(\varepsilon_{33} - 1)\}, \qquad \text{(eqn 2.39)}$$

and the index of refraction change along the a-axis is

$$\delta (n_1) = \{n_1 3 \, r_{13} \, \delta P_3\} / \{2(\varepsilon_{33} - 1)\}. \qquad \text{(eqn 2.40)}$$

In these equations, ε_{33} is the dielectric constant in the direction of the c axis; and $r_{13} = r_{113}$ and $r_{33} = r_{333}$ are the electrooptic coefficients along the a axis and along the c axis, respectively. Johnston's [Ref. 26] model does not fully explain photorefraction, because of the following problems: 1) It can not explain the existence of the bulk photovoltaic steady-state current. 2) According to this model, the open circuit photovoltage should decay with the dielectric relaxation time of the crystal. In reality, this voltage eventually reaches a steady-state value (see Figure 2.8). 3) This model requires an extremely high density of free electrons to cause photorefraction. Overall, this model should be modified by taking into account the major cause of photorefraction, which we already know is the photo-induced space-charge field that resultes from the charge transport mechanisms. Following Kukhtarev et al. [Ref. 2], the photo-induced refractive index modulation is

$$\delta (n_3) = (1/2) n_3^3 r_{33} E_{sc} , \qquad \text{(eqn 2.41)}$$

and

$$\delta (n_1) = (1/2) n_1^3 r_{13} E_{sc} . \qquad \text{(eqn 2.42)}$$

G. PHOTOREFRACTIVE EFFECT IN $BATIO_3$

Several mechanisms that result in photorefraction, were mentioned in the previous sections. In this section, all these ideas will be put together, in order to explain photorefraction. Since beam-coupling is a significant manifestation of photorefraction, it will be taken as an example.

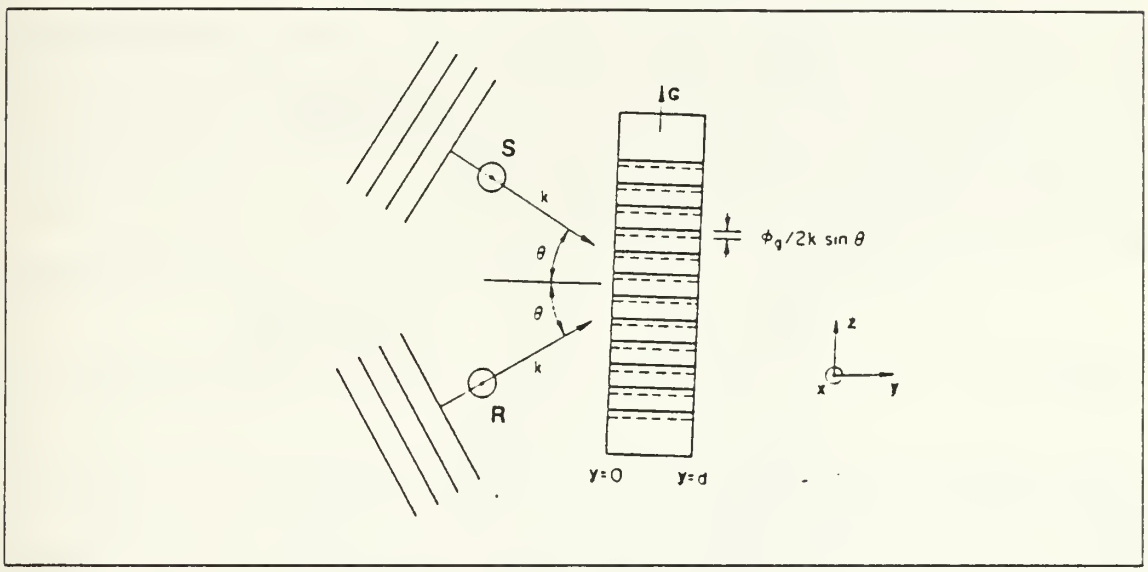

Figure 2.16 Formation of interference pattern [Ref.27].

As is seen from Figure 2.16, the interaction of two coherent beams (S: signal beam, R: reference beam) crossing at $2\theta_0$ (refraction angle) creates an intensity interference pattern along the c-axis. As we see from Figure 2.16 the fringe spacing can be varied by changing the incident angle θ . The wave number of this pattern is $K_g = 2k\sin\theta$, where k is the wave number of the incident beam $k = 2\pi/\lambda$. The intensity interference pattern can be expressed by

$$I(z) = I_0 (1 + m\cos K_g z). \qquad \text{(eqn 2.43)}$$

In this equation, I_0 is the total intensity of each of the two waves,and m is the modulation ratio. Under the absorption of light, electrons will be excited from filled donors to the conduction band and holes will be excited from acceptors to the valence band. Photocarriers will have the same perodicity as the interference pattern. These photocarriers will migrate to the dark regions, under the influence of diffusion, drift

and the BPVE mechanisms. Then, charges recombine with empty traps. Charge transport results in a space-charge grating. This periodic space-charge distribution has the same spatial frequency as the intensity interference pattern. But, in general, the space-charge grating is out of phase with the interference pattern.

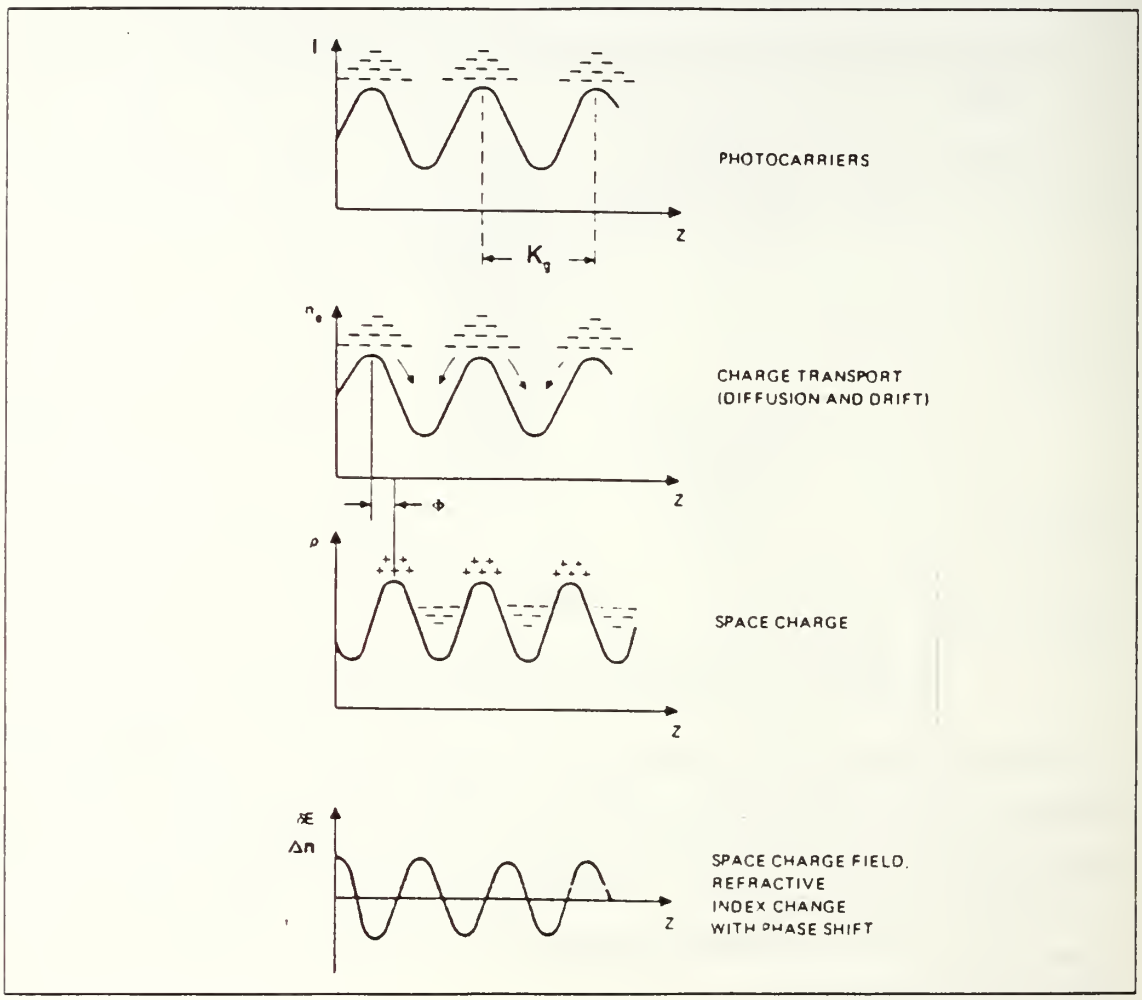

Figure 2.17 Photorefraction due to beam-coupling [Ref.18].

This photo-induced space-charge distribution ρ (z) results in a periodic space-charge field E_{sc} as a result of Poisson's equation. Young et al. [Ref. 28] found an expression for the photo-induced space-charge field E_{sc} , without including the contribution of holes to the charge transport processes. For the case in which diffusion is the only transport mechanism, E_{sc} is given by

$$E_{sc}(z,t) = \{(eg(z,t)tm)/\varepsilon\}\{(KL_d^2)/(1+(KL_d)^2)^{1/2}\}\sin Kz . \qquad \text{(eqn 2.44)}$$

For the case of drift alone, E_{sc} is given by

$$E_{sc}(z,t) = -\{(eg(z,t)tm)/\varepsilon\}\{L_e/(1+(KL_e)^2)^{1/2}\}\cos(Kz+\varphi_e). \qquad \text{(eqn 2.45)}$$

For the case of BPVE alone, E_{sc} can be expressed by

$$E_{sc}(z,t) = \{(eg(z,t)tm)/\varepsilon\}\{L_{ph}/(1+(KL_{ph})^2)^{1/2}\}\cos(Kz-\varphi_{ph}). \qquad \text{(eqn 2.46)}$$

In the last three equations, $K = K_g$ is the interference pattern wave number, g(z,t) is the charge generation rate, and $\varepsilon = \varepsilon_{33}$ is the extraordinary dielectric constant. L_d, L_e and L_{ph} are transport lengths in diffusion, drift and in the BPVE processes, respectively. The φ_e and φ_{ph} are phase shifts from the interference pattern due to drift and the BPVE processes, respectively. The relations between transport lengths and phase shift angles can be written in this fashion

$$\varphi_{ph} = \tan^{-1} KL_{ph}, \quad \varphi_e = \tan^{-1} KL_e. \qquad \text{(eqn 2.47)}$$

In the last equation, the charge transport length in the BPVE prosess is given by $L_{ph} = l_+ p_+ - l_- p_-$. From these relations, it can be seen that phase of the E_{sc} is strongly dependent on the transport length in the process. If diffusion dominates over the other mechanisms in the general charge transport, then it leads to a phase shift of 90° between the space-charge field and the intensity pattern. This can be seen comparing Equation 2.43 with Equation 2.44.

Finally, the space-charge field modulates the index of refraction via the electrooptic (Pockel) effect. But, we know that there are small (negligible) contributions of polarization changes to photorefraction, given by Equation 2.39

$$\delta(n_3) = (1/2)n_3^3 r_{33}\{E_{sc}(z,t) + \delta P_3/(\varepsilon_{33}-1)\}. \qquad \text{(eqn 2.48)}$$

Since E_{sc} is out of phase with I(z),the refractive index change will also be out of phase. This phase shift between the interference pattern and refractive index pattern (its magnitude depends on the charge transport mechanism), causes energy tranfer between the two beams. This is the so called beam-coupling. All these ideas can be summarized in Figure 2.17 If the incident beam intensities are not equal during the beam-coupling,

energy will be transferred from the strong beam to the weak beam. Valley [Ref. 24] assigns the direction of the energy transfer according to the type of carriers involved in the charge transport. For the geometry depicted in Figure 2.16, if the energy transfer is from the reference beam to the signal beam, then the majority carriers are holes. But if the energy transfer is reversed, then the majority carriers are electrons. Beam-coupling and energy transfer are strongly dependent on the transport length of the charge transport process.

COUPLED WAVE THEORY: This is another way to explain beam coupling. If the Bragg condition is satisfied, the hologram grating will diffract the incident beams. The fraction of the incident light which is diffracted is related to the amplitude of the sinusoidally varying index change δ n. Kogelnik [Ref. 29] has given a relation for the diffraction efficiency η

$$\eta = \sin^2 (Ml), \qquad \text{(eqn 2.49)}$$

where $M = \pi \delta n / \lambda \cos\theta_0$. Here, δ n is the magnitude of the index of refraction change, l is the interaction length of the two beams, λ is the wavelength of the incident light and θ_0 is the angle of refraction. The interaction length is comparable to the crystal thickness and can be considered as the thickness of the hologram grating. Amodei et al., [Ref. 30] have applied coupled-wave theory to the beam-coupling problem. Important aspects of this work are given by

$$\{I_r^{\,l} / I_s\} = \cos^2 (Ml) + A^2 \sin^2 (Ml) - A\sin(2Ml)\sin\varphi \,, \qquad \text{(eqn 2.50)}$$

and

$$\{I_s^{\,l} / I_s\} = \sin^2 (Ml) + A^2 \cos^2 (Ml) + A\sin(2Ml)\sin\varphi \,. \qquad \text{(eqn 2.51)}$$

In the last two equations, $I_r^{\,l}$ is the intensity of the strong beam exiting the crystal, when the weak beam is turned on. $I_s^{\,l}$ is the intensity of the weak beam exiting the crystal when the strong beam is turned on. I_s is the intensity of weak beam exiting the crystal, when the strong beam is turned off. A is the ratio of I_s to I_r , where I_r is the intensity of strong beam exiting the crystal when the weak beam is turned off. If we subtract the last two equations from each other, having used the fact that $I_r^{\,l} = I_r - \Delta I$

and $I_s^1 = I_s + \Delta I$, then an amount of energy ΔI is transferred from the strong beam to the weak beam, as given by the relation [Ref. 30]:

$$(1/A)-2F-1=(1-A^2)\cos(2Ml)-2A\sin(2Ml)\sin\varphi \ . \qquad \text{(eqn 2.52)}$$

In this equation, $F=\Delta I/I_s$ is called the fractional energy transfer, and the relation between the fractional energy transfer and diffraction efficiency is given by

$$\{\Delta I/I_s\}=2\eta^{1/2} \ . \qquad \text{(eqn 2.53)}$$

H. DERIVATION OF THE QUANTUM EFFICIENCY OF $BATIO_3$

In this section, the pyroelectric effect, bulk photovoltaic effect and results of coupled wave theory will be used to determine the quantum efficiency of $BaTiO_3$. There have been some attempts to find the quantum efficiency of ferroelectric semiconductors in the literature. Glass et al. [Ref. 31] found a quantum efficiency 0.17 for $LiNbO_3$. A diffraction efficiency method was used to get that number. As they noted, a quantum efficiency of 0.17 gave a trapped electron density that was three times the Fe concentration of the crystal (impossible). Later, Young et al. [Ref. 32] found a quantum efficiency of $\sim 10^{-3}$ for $LiNbO_3$. They first estimated the photovoltaic transport length, and using Equation 2.15, calculated the quantum efficiency.

First, using electrostatics, we shall derive the pyroelectric current equation.

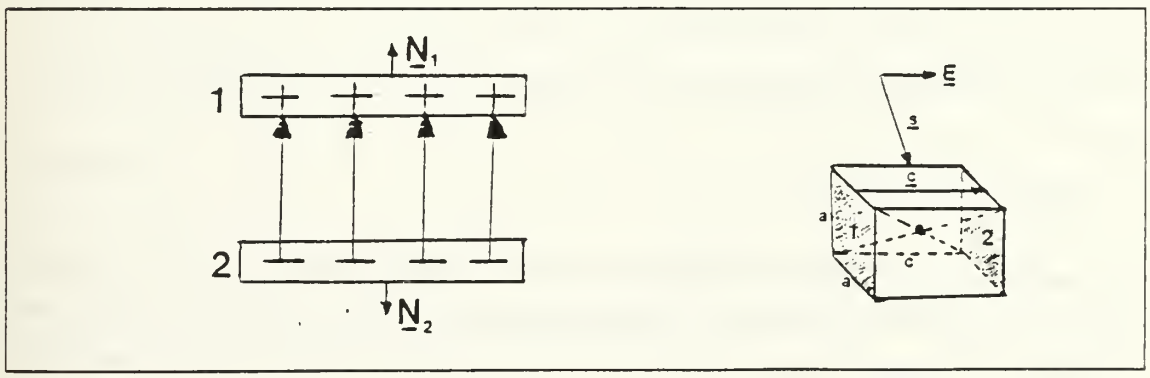

Figure 2.18 Polarization surface charges.

Figure 2.18 is appropriate for a single domain crystal. This means the volume polarization charge density is zero ($\rho_p = -\nabla \cdot \underline{P}_s = 0$). On the other hand, the polarization charge densities on the surfaces are not zero but are given by

$$\underline{P}_s \cdot \underline{N}_1 = \rho_{p1} \text{ and } \underline{P}_s \cdot \underline{N}_2 = \rho_{p2} . \qquad \text{(eqn 2.54)}$$

In the last equation, $\underline{N}_1$ and $\underline{N}_2$ are unit vectors normal to the surfaces; while $\rho_{p1} = q_{p1} / A_{s1}$ and $\rho_{p2} = q_{p2} / A_{s2}$ are polarization surface charge densities. In our crystal the surface areas are equal, $A_{s1} = A_{s2} = A_s$ From the relations above, the surface polarization charges are

$$q_{p1} = P_s A_s \text{ and } q_{p2} = -P_s A_s . \qquad \text{(eqn 2.55)}$$

When the crystal was illuminated, the crystal warmed up and as a result expanded the unit cell. This expansion caused a change in the spontaneous polarization. If the rate of change in temperature was large enough, a pyroelectric current,

$$i_{py} = (dq_p / dt) = A_s (dP_s / dt) \qquad \text{(eqn 2.56)}$$

occured. The change in P_s was due to heating,

$$(dP_s / dt) = (dP_s / dT)(dT/dt). \qquad \text{(eqn 2.57)}$$

Invoking this equation in Equation 2.56 gives

$$i_{py} = A_s (dP_s / dT)(dT/dt). \qquad \text{(eqn 2.58)}$$

Using the definition in Equation 2.13, we can rewrite the last equation in the form

$$i_{py} = A_s p(T)(dT/dt), \qquad \text{(eqn 2.59)}$$

where p(T) and (dT/dt) are the pyroelectric coefficient and the rate of temperature change, respectively. We need to know how much power was absorbed to produce this current. We can find this with a thermodynamic relation. Thermodynamically the

absorbed power equals the heat to warm up the crystal minus the radiative heat loss. The radiative heat loss obeys the Wien radiation law and is negligible because of the low power range in the experiments: the crystal temperature did not change significantly with respect to room temperature ($\sim$ 9°C). The absorbed power per cm (Φ) can be written as

$$\Phi = JC_p \rho A_b (dT/dt), \qquad \text{(eqn 2.60)}$$

where C_p is the specific heat of the crystal at constant pressure, A_b is the beam area, J is the mechanical equivalent of heat (i.e., Joules per Calorie), and ρ is the density of $BaTiO_3$. We can rewrite the last equation, combining it with the pyroelectric equation, as

$$\Phi = \{(JC_p \rho)/p\}(A_b / A_s) i_{py} . \qquad \text{(eqn 2.61)}$$

The last equation relates the absorbed power per cm (Φ) to the pyroelectric current. The next step was to find the number of absorbed photons per second per cm (N_p)

$$N_p = (\Phi / h\nu) \sec^{-1} \text{cm}^{-1} . \qquad \text{(eqn 2.62)}$$

In the last equation, h is Planck's constant, and ν is the frequency of the incident beam. In order to find the quantum efficiency, we need to know the number of photo-excited carriers, corresponding to N_p . During our photo-induced current measurements, an external field was not applied (see Section III-B). This means, in the general charge transport Equation 2.25, that the first term is zero. The remaining two terms in this equation are due to diffusion and BPVE. The absorption coefficient measurements showed that the impurities are anisotropically distributed in the crystal (see section III-A). As already discussed in Section II-C, the BPVE is due to the anisotropically distributed impurities in the crystal. In fact a short circuit photovoltaic current was observed in the steady-state in our photocurrent measurements (see Section III-B). Moreover, Kratzig et al. [Ref. 33] were able to reduce the photorefraction (optical damage) by compensating for the BPVE. This indicates that the BPVE will be the key component in the quantum efficiency. If we rewrite Equation 2.15, and using 2.17, then the photo-excited carriers per cm per second N_c is

$$N_c = (i_{ph} / L_{ph}\, e)(A_b / A_s). \qquad \text{(eqn 2.63)}$$

In this equation, i_{ph} is the SCPVC, L_{ph} is the transport length in the photovoltaic process, defined under equation 2.47, and e is the electronic charge. The quantum efficiency is given by

$$Q = (N_c / N_p). \qquad \text{(eqn 2.64)}$$

Rearranging Equation 2.65 in terms of L_{ph} we have

$$QL_{ph} = (i_{ph} / \Phi\, e)(h\nu)(A_b / A_s)\ \text{cm}. \qquad \text{(eqn 2.65)}$$

The surface area of our crysatal is $A_s = 0.25\text{cm}^2$. The diameter of the beam, defined by the e^{-2} value of its intensity is 1.3mm (as given by the manufacturer). This gives $A_b = 0.0132\text{cm}^2$. The rest of the parameters involved in Equation 2.62 can be read from Table 1. Using J = 4.26 (Joule/calorie), $C_p = 0.12$ (calorie/gram °C), $\rho = 6$ (gram/cm^3) and $p = 2*10^{-8}$ (Coulomb/cm^2), Equation 2.62 becomes

$$\Phi = 0.0792*10^{+8}\, i_{py} = \alpha_p\, W \quad \text{Watt/cm}. \qquad \text{(eqn 2.66)}$$

In the last equation W is the incident beam power and α_p is the photorefractive absorption coefficient. Rewriting Equation 2.18 as

$$i_{ph} = \kappa\, \alpha_p\, W(A_s / A_b), \qquad \text{(eqn 2.67)}$$

and using Equation 2.67 we find the anisotropy constant κ to be

$$\kappa = (i_{ph} / \Phi)(A_b / A_s)((\text{Ampere-cm})/\text{watt}). \qquad \text{(eqn 2.68)}$$

If we rewrite Equation 2.66, it becomes

$$QL_{ph} = \kappa\, (\nu)\, ((h\nu)/e)\ \text{cm}. \qquad \text{(eqn 2.69)}$$

This relation was used by Young et al. [Ref. 34] and Vahey [Ref. 35], but they all took large values for the absorption coefficient in the calculation of the quantum efficiency of $LiNbO_3$. To the best of our knowledge, this is the first reported calculation of Q for $BaTiO_3$.

The next task was to find the carrier transport length L_{ph} in the photovoltaic process. The results of coupled wave theory were used. As already stated, the amount of energy transferred from the strong beam to the weak beam depends on the phase angle between the hologram grating and the interference pattern. This phase angle in turn is determined by the carrier transport length L_{ph} . If Equation 2.53 is rearranged, the phase shift angle φ is

$$\varphi = \sin^{-1} \{(1-A^2)\cos(2Ml)-((1/A)-2F-1)\}/\{2A\sin(2Ml)\}. \qquad \text{(eqn 2.70)}$$

Since BPVE dominates in the general charge transport equation (due to Equation 2.46), $\varphi = \varphi_{ph}$. Arranging Equation 2.47, the charge transport length is

$$L_{ph} = (1/K)(\tan\varphi_{ph}). \qquad \text{(eqn 2.71)}$$

Combining the last equation with Equation 2.70, the quantum efficiency is

$$Q(\nu) = (\kappa(\nu)h\nu K)/(e\tan\varphi_{ph}). \qquad \text{(eqn 2.72)}$$

In the last equation, Q is the quantum efficiency, K is the wave number of the grating, h is Planck's constant, ν is the frequency, e is the electronic charge and φ_{ph} is the angle between the hologram grating and the intensity pattern.

In order to find an actual number for the quantum efficiency Q, we need to have the values of the photorefractive absorption coefficient α_p , the short circuit photovoltaic current i_{ph} , the pyroelectric current i_{py} and the phase shift angle between the hologram grating and the intensity grating φ_{ph} . These parameters had to be obtained from experiments. The photocurrent measurements were made to determine α_p , i_{py} and i_{ph} . Beam-coupling measurements were made to determine φ_{ph} . In the next chapter, the experimental methods related to the microscopic parameters mentioned above will be presented. At the end of the next chapter, the quantum efficiency will be calculated, using the theory presented here, and the experimentally determined parameters.

TABLE 1

MICROSCOPIC PARAMETERS OF $BATIO_3$

PARAMETER	SYMBOL	VALUE	REFERENCES
Size of tetragonal	c	4.036A°	[Ref.2]
unit cell.	a	3.992A°	"
Dielectric	ε_c	160	[Ref.6]
constant	ε_a	4100	"
Mag.of spon. pol.vector.	P_s	$16*10^{-6}$ Coulomb cm^{-2}	"
Mass density	ρ	6 gr cm^{-3}	[Ref.9]
Specific Heat	C_p	0.12 cal/gr°C	"
Mec.Eq.of Heat	J	4.16 Joule/calorie	"
Pyroelectric coef.	p	$2*10^{-8}$ Coulomb cm^{-2}	"
Index of	n_o	2.437	[Ref.2]
Refraction	n_e	2.365	"
Electrooptic	r_{11}	8 pm/V	[Ref.35]
	r_{33}	23 pm/V	"
coefficients	r_{42}	820 pm/V	"
Recomb.cons.	γ_r	$5*10^{-8}$ cm^3 /sec	[Ref.35]
Mobility	μ	0.5 cm^2 /Vsec	[Ref.34]

III. EXPERIMENTAL OBSERVATIONS

A. ABSORTION COEFFICIENT MEASUREMENTS

1. Purpose of this experiment

Absorption coefficient measurements play an essential role in identifying the types of impurities in a crystal. However, it is not the only method since EPR measurements can achieve for the same purpose [Ref. 18]. Our interest is photorefraction and the subsequent beam-coupling at visible wavelengths. Absorption coefficient measurements are helpful in identifying the the band gap and the type of impurities in semiconductor crystals. If one had access to a crystal doping facility, one could dope the crystal with a suspected impurity and observe the effect on the absorption spectra. Unfortunately, we did not have the doping facilities to do this. Absorption coefficient measurements helped us find the energy band gap and to understand the molecular vibration modes in $BaTiO_3$. The infrared absorption spectrum gave information on the vibrational motion of the Ti^{4+} -O^{2-} ions, which are the ions responsible for spontaneous polarization. Not all of the absorbed energy contributes to photorefraction. We suspect that some of the absorbed energy is lost on the internal reflections, scattering and etc.

2. Procedure

Ultraviolet (UV), visible and near infrared (NIR) absorption coefficient measurements were made by using a Perkin-Elmer Model 330 spectrophotometer. It covers the 187-2500nm wavelength range and the wavelength accuracy is 0.2nm for the UV region and 1nm for the NIR region. The output light beam of this instrument was partially polarized. For our purposes, polarized light was needed. Therefore, a polarizer was used to get horizontally polarized light. The spectrophotometer beam size was larger than the crystal size, so a special holder was used to confine the light beam to the crystal size.

In order to measure the absorption coefficient of the crystal, the absorption due to the polarizer and holder had to be eliminated. This was achieved by simply making a correction run before the measurement. Therefore, without the crystal, the instrument indicated zero absorption.

In the infrared (IR) region of the spectrum, absorption coefficient measurements were made by using a Perkin-Elmer Model 337 IR spectrophotometer. This has a 2.5-25μ m wavelength range. In this case, a polarizer was not used but a beam restricting aperture was used. This instrument was not computerized, so a correction run was not needed. Instead, a shutter was used on the reference beam path, and then the gain of the instrument was adjusted to give zero absorption without the crystal in the signal beam path. These spectrophotometers measure the absorbance, which is dimensonless. In order to get a absorption coefficient α , this relation has to be used α = Absorbance/crystal length . Our crystal is 0.5 cm long. Then the absorption coefficient α = (2*Absorbance)cm^{-1} .

The reflection loss from a surface of index of refraction n is given by

$$R=(n-1)^2/(n+1)^2 . \qquad \text{(eqn 3.1)}$$

In this equation R is the ratio of the reflected beam intensity to the incident beam intensity and n is the index of refraction at a wavelength where the crystal is nonabsorbing. R does not vary appreciably with wavelength. Using n = 2.4, R was found to be 0.17 [Ref. 36]. In the calculation of quantum efficiency, the absortion coefficient obtained from this method were not used, instead we used absorption coefficients derived the pyroelectric measurements. Because of this, Fresnel reflection losses were not removed from data. These measurements were made at a room temperature of 23°C.

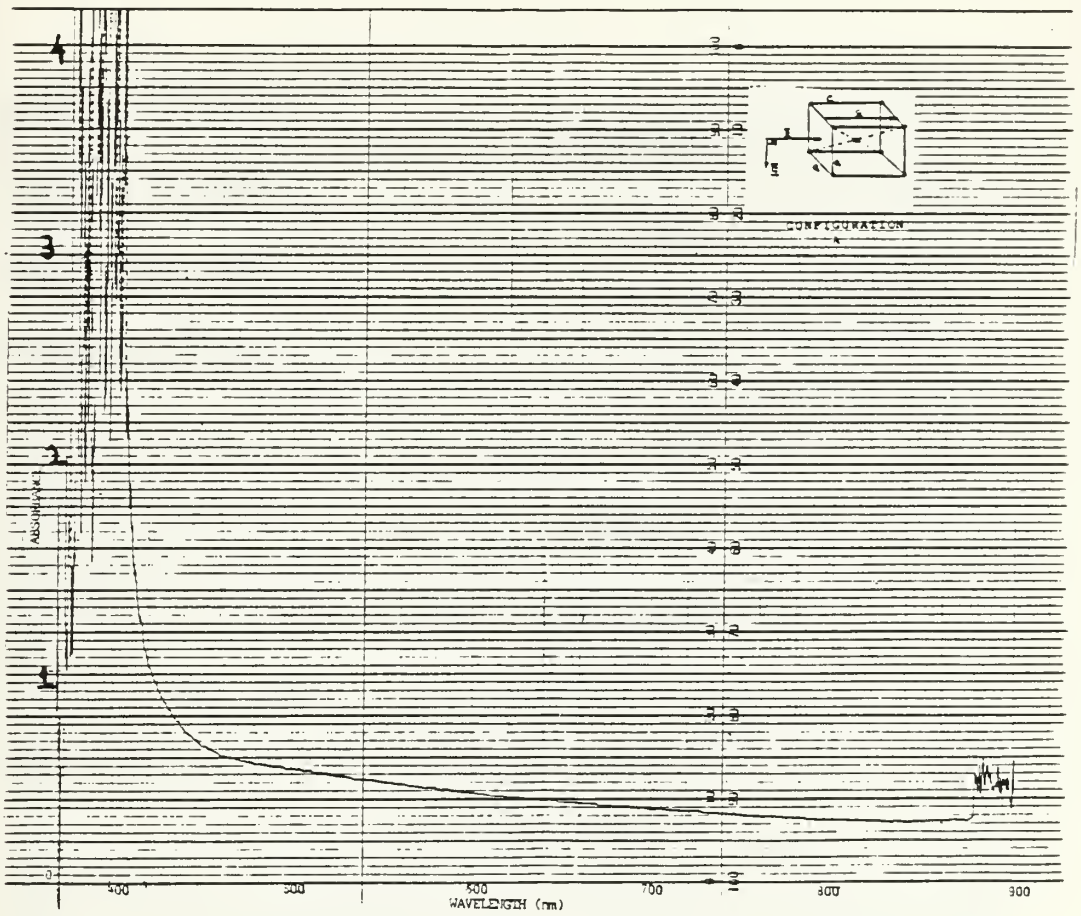

Figure 3.1 Measured absorption spectrum of $BaTiO_3$, $\underline{E} \perp c$, $\underline{K} // c$.

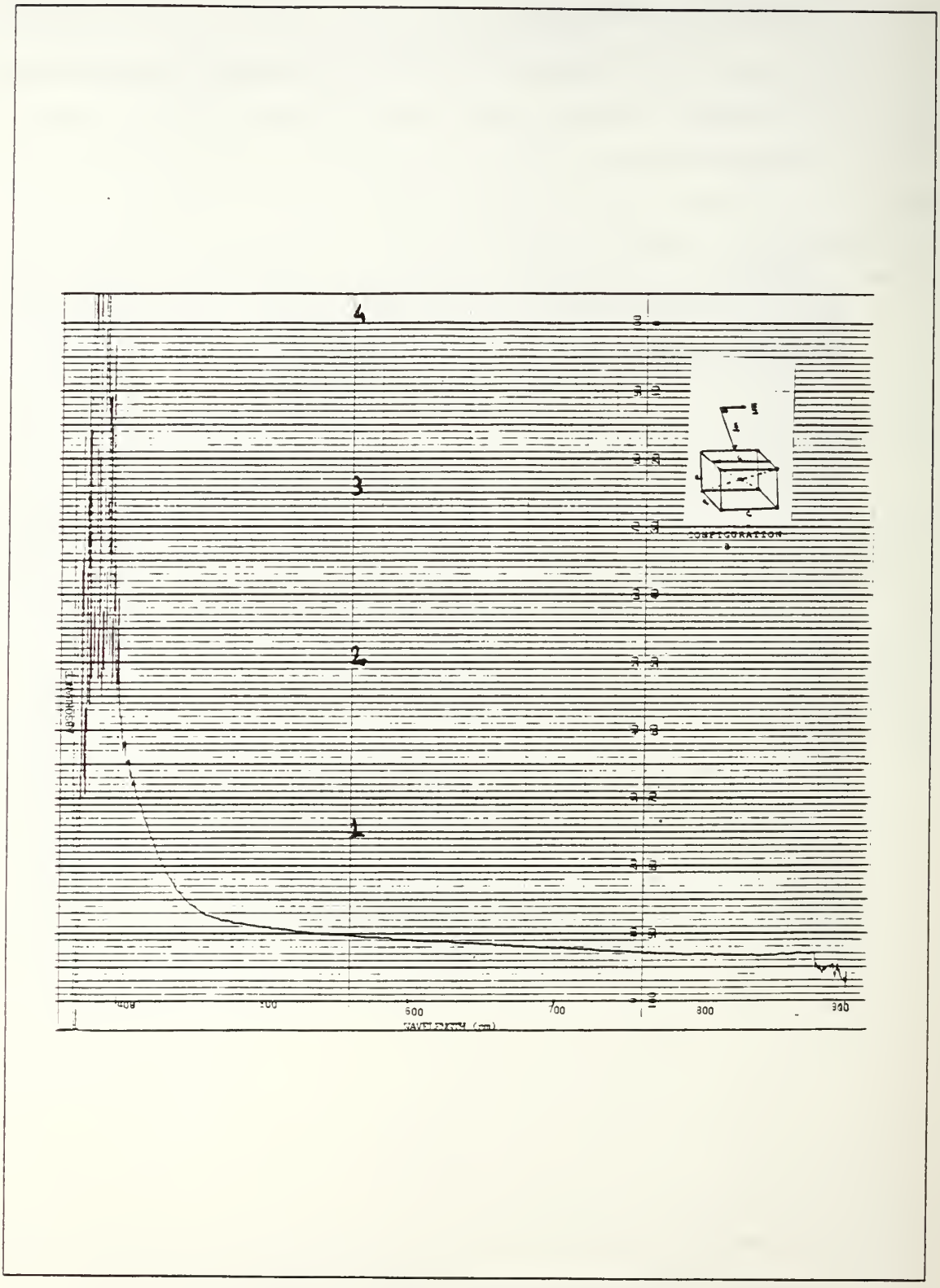

Figure 3.2 Measured absorption spectrum of $BaTiO_3$, $\underline{E} \perp c$, $\underline{K} // c$.

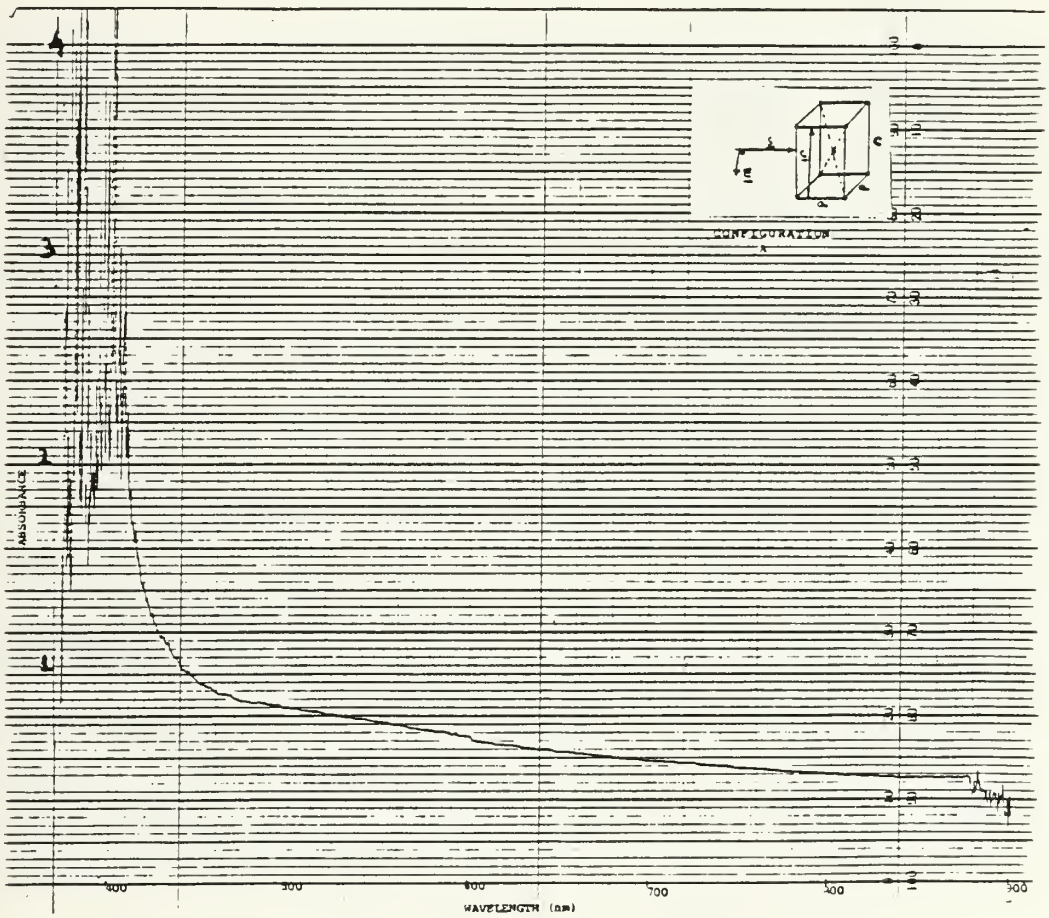

Figure 3.3 Measured absorption spectrum of $BaTiO_3$, $\underline{E} \perp c$, $\underline{K} \perp c$.

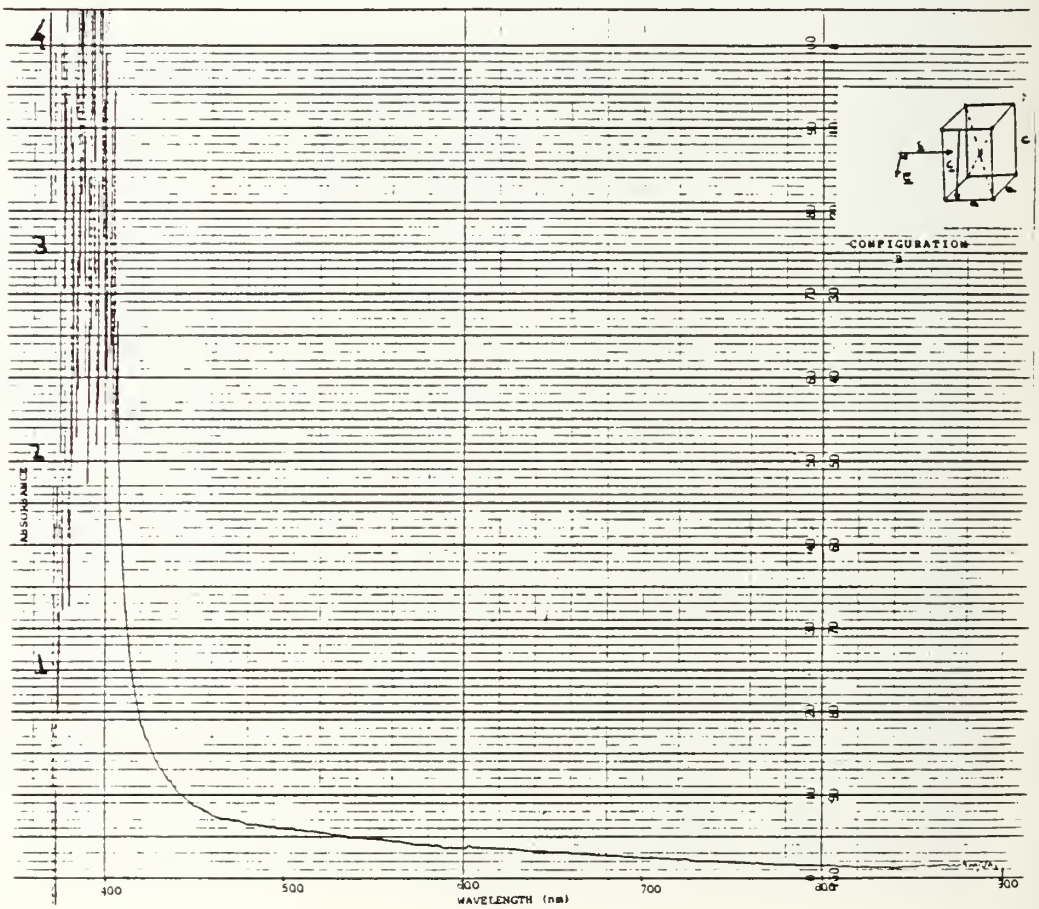

Figure 3.4 Measured absorption spectrum of $BaTiO_3$, $\underline{E} \perp c$, $\underline{K} \perp c$.

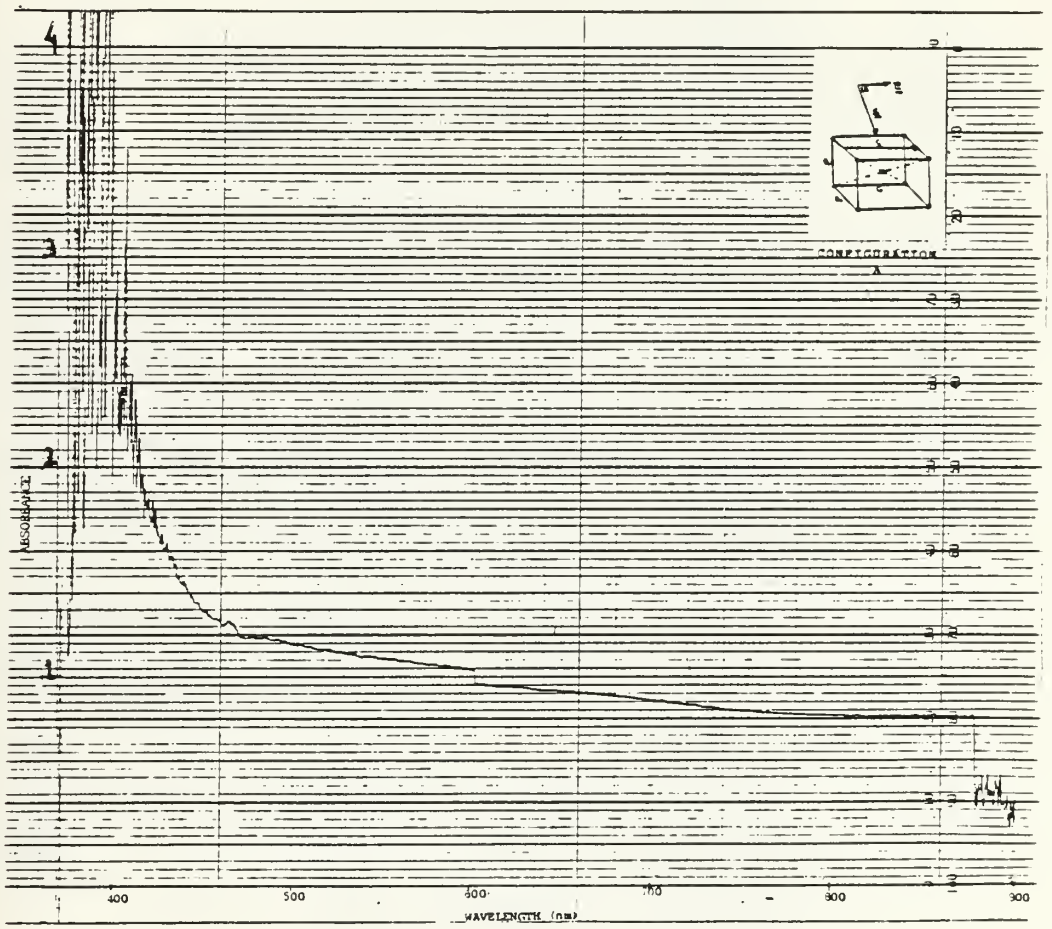

Figure 3.5 Measured absorption spectrum of $BaTiO_3$, $\underline{E}$ // c, $\underline{K} \perp$ c.

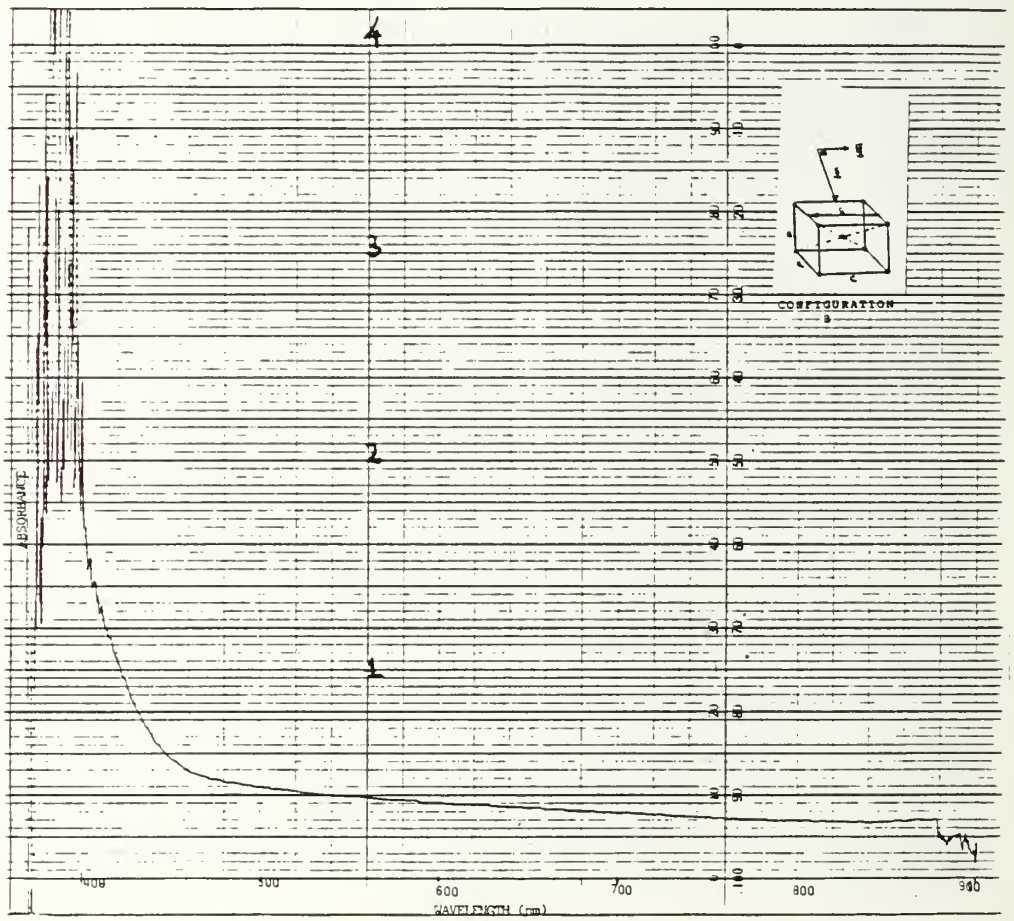

Figure 3.6 Measured absorption spectrum of $BaTiO_3$, $\underline{E}$ // c, $\underline{K} \perp$ c.

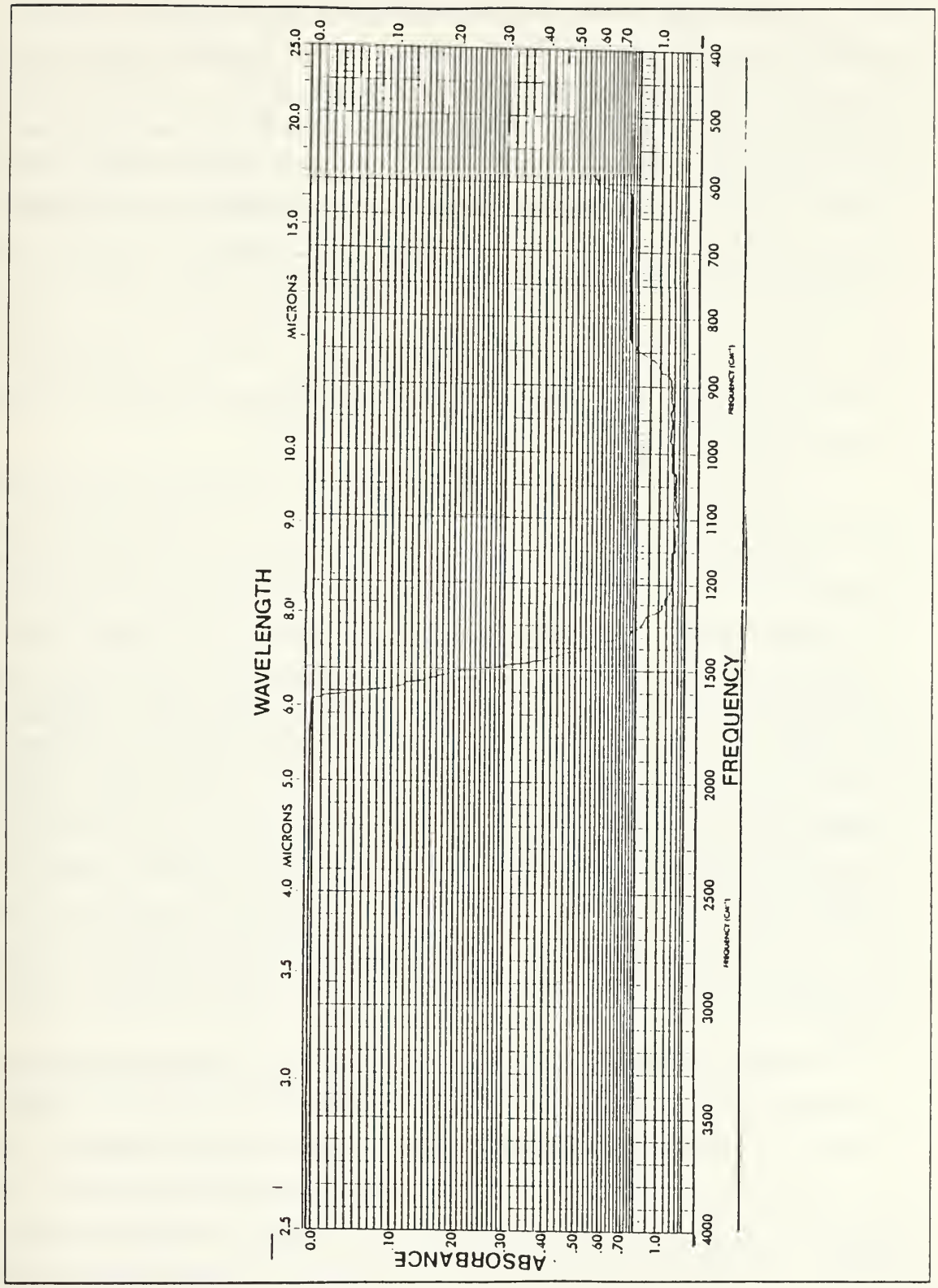

Figure 3.7 Measured absorption spectrum of $BaTiO_3$ at IR region.

4. **Interpretation of the results**

As we see from Figure 2.5, the dielectric constant of $BaTiO_3$ is anisotropic in other words, ε_a is not equal to ε_c . Because of the tetragonal crystal symmetry we can expect anisotropic absorption coefficients for $BaTiO_3$. In the 370-900nm wavelength range, the absorption coefficient measurements were made at six different crystal orientations. The electric field of the incident beam can be either parallel or perpendicular to the c axis of the crystal in these configurations. For instance, in Figure 3.1 and 3.2, $\underline{E} \perp$ c and $\underline{K}$ // c , where $\underline{K}$ is the propagation direction, but the c axis direction was reversed in Figure 3.2. In Figure 3.3 and 3.4, $\underline{E} \perp$ c, $\underline{K} \perp$ c, but the c axis direction was reversed in the second one. In Figure 3.5 and 3.6, $\underline{E}$ // c and $\underline{K} \perp$ c but in Figure 3.6, the c axis direction was reversed. For each configuration, the absorption spectrum was different. This is an indication of the anisotropic absorption center (impurity) distribution.

Common characteristics of Figure 3.1-3.6 are: 1) There is a broad absortion plateau between 880nm and the band edge at 460nm. 2) The maximum absorption is at $\sim$ 410nm, which gives us the band gap energy. Feinberg et al. [Ref. 19] showed that the absorption plateau became smaller after the crystal had been treated with 0.2 atm of O_2 . The band-edge shifted to shorter wavelengths, as the oxygen pressure of the process was increased, indicating that the band gap was increased by the presence of oxygen vacancies. From this argument and our experimental results, it appears that our crystal was treated with low oxygen pressure (below 0.5atm) and therefore the density of oxygen vacancies is low (see Figure 2.12a). The largest absorption coefficient was obtained in Figure 3.5. In this configuration, $\underline{E}$ // c and the absorption coefficient at 500nm was $\alpha = 2.32\ cm^{-1}$. The lowest absorption coefficient was obtained when $\underline{E} \perp$ c in Figure 3.4 and absorption coefficient α at 500nm was $\alpha = 0.88\ cm^{-1}$. The band gap energy can be found from the absorption spectrum. The band gap energy for the $\underline{E}$ //c case is $E_g = (hc/\lambda_g) = 3.08eV$ and for the $\underline{E} \perp$ c case it is 3.15eV.

In the 900-2500nm wavelength range no major absorption was observed. Consequently, the absorption spectrum in this region was not included. As seen from Figure 3.7, the absorption coefficient was zero between 2.5μ m and 6.05μ m, and there is a broad absorption band between 8μ m and 15μ m where the absorption is quite high ($\sim$ 10 cm^{-1}). Last [Ref. 37] discussed the infrared absorption mechanism in $BaTiO_3$. If a $BaTiO_3$ crystal contains N unit cells, and each unit cell has five atoms,

the crystal has 15N degrees of freedom. In this case, 3N degrees of freedom relates to translational motion and 3N to torsional motion of the unit cell. The remaining 9N modes are related to vibrational degrees of freedom. The nine vibration modes of the unit cell can be classified into the three vibrations of Ba against the TiO_3 group and six internal TiO_3 vibrations. TiO_3 group was considered as a single atom situated at the Ti position. The six vibrations of Tio_3 reduce to two IR active vibrations.

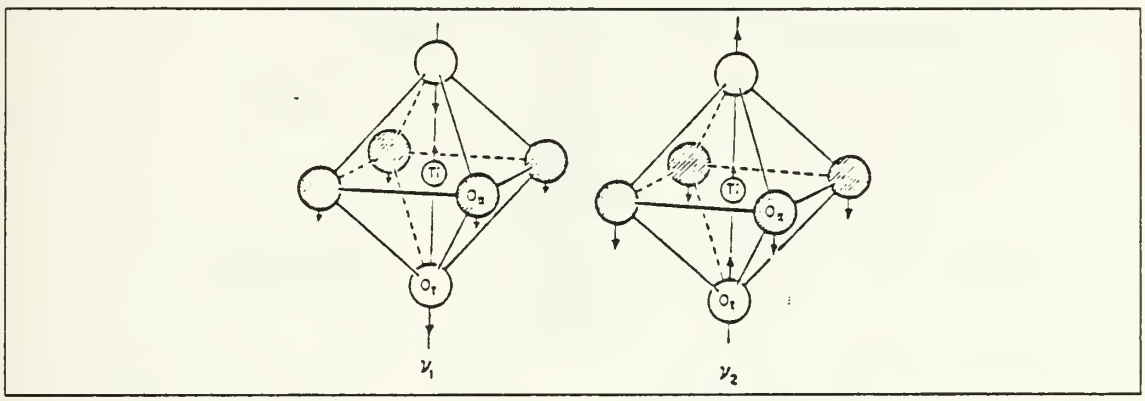

Figure 3.8 IR active normal vibrations of a TiO_6 octahedron [Ref.33].

In Figure 3.8, the high frequency stretching ν_1 and lower frequency bending ν_2 vibrations are illustrated. The stretching vibration is due to a change in length of Ti-O_1 bond and the bending vibration is due to a change in the O_2 -Ti-O_1 bond angle. Then vibrational motions are primarily motions of oxygen ions. Last [Ref. 37] reported two absorption bands, one between 15-20μ m and another one around 20-30μ m for cubic $BaTiO_3$. He concluded that the 15-20μ m band is due to stretching vibration and 20-30μ m band is due to bending vibration. For the tetragonal unit cell, he observed only the stretching vibration at 9-20μ m. Our results showed a broad absorption band at 8-15μ m. This band is at higher frequencies than Last's. This may be due to the poling process performed during the crystal manufactured. Poling decreased the Ti-O_1 distance which increased the vibrational frequency.

B. PHOTOCURRENT MEASUREMENT EXPERIMENTS

1. Purpose of this experiment

Photocurrent measurements were made to determine the pyroelectric effect and the bulk photovoltaic effect (BPVE). In order to determine the quantum efficiency in $BaTiO_3$, we needed to measure the pyroelectric current and the short circuit photovoltaic current (SCPVC).

2. **Procedure**

During these experiments, a Lexel Model 95 Ar^+ laser was used as a coherent light source. It was operating on a single transverse mode but on multi longitudinal modes. For the photocurrent measurements, a single longitudinal mode laser light was not vital. The output beam from the laser was 1.3mm diameter and vertically polarized. In order to avoid the photon drag effect, platinum electrodes (the area of the electrodes was $0.25cm^2$) were attached to the polar faces of the crystal which were perpendicular to the c axis and parallel to the laser beam (see Figure 3.9).

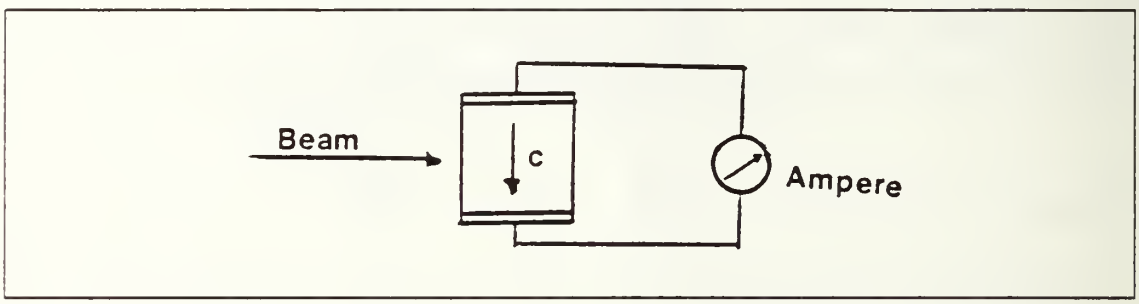

Figure 3.9 Experimental set up.

The crystal was mounted on a protoboard and this system was shielded by an aluminum box in order to reduce enviromental interference. In this setup, the c axis of the crystal was always parallel to the electric field of the incident beam. The short circuit current measurements were made with a Keithley 617 electrometer and its output feed a Hawlett-Packard 7090A plotter. These experiments were made at night time in the dark, in order to avoid stray light from the environment. For convenience, 200sec duration light pulses were used. A black card was used to chop the incident laser light. Photo-induced currents were measured at three different wavelengths (514.8nm, 488nm, 457.9nm) and three different incident laser power (25mW, 50mW, 75mW) at each wavelength for two different configurations. The measurements were made at a room temperature of 23°C.

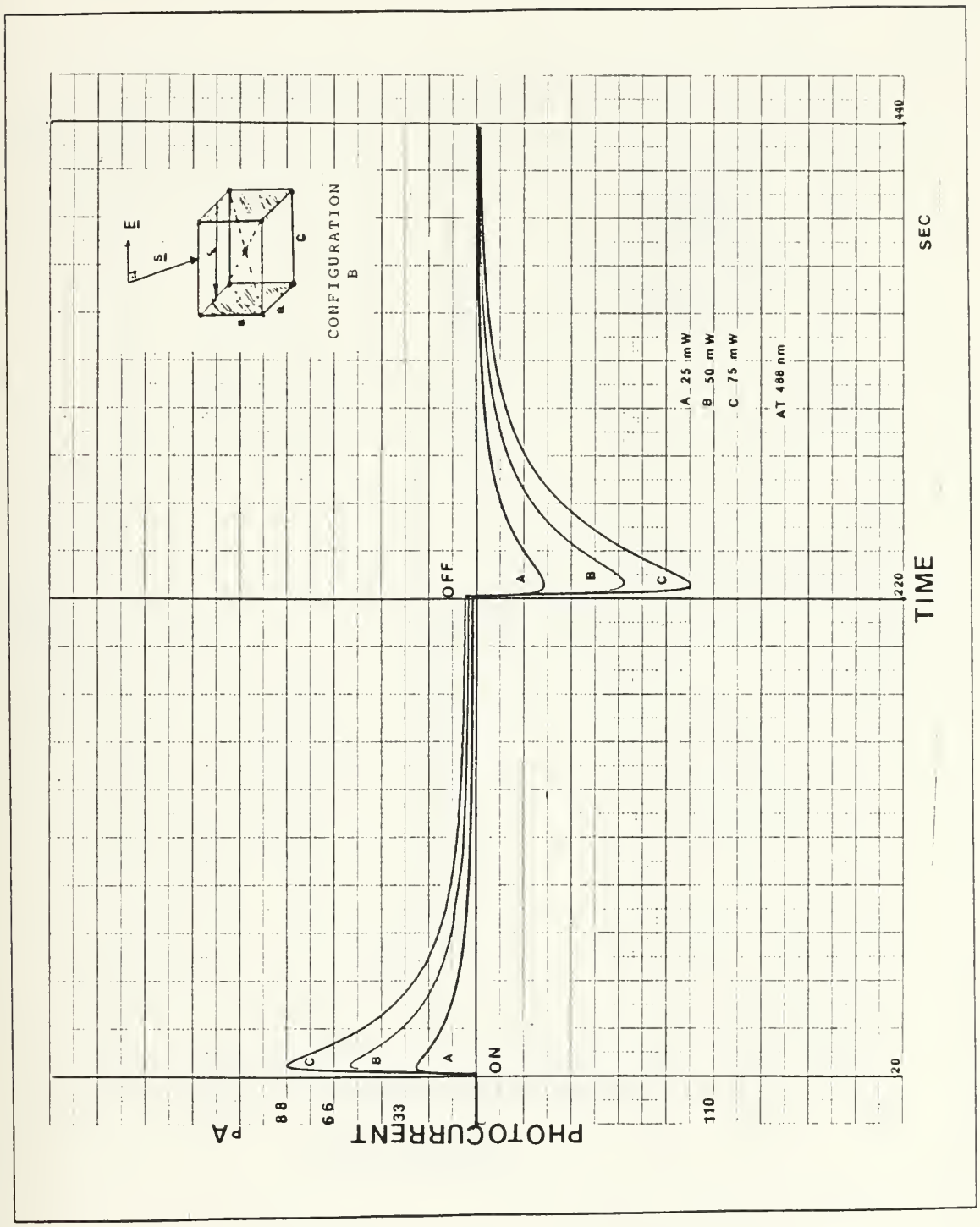

Figure 3.10 Measured photocurrent along +c axis.

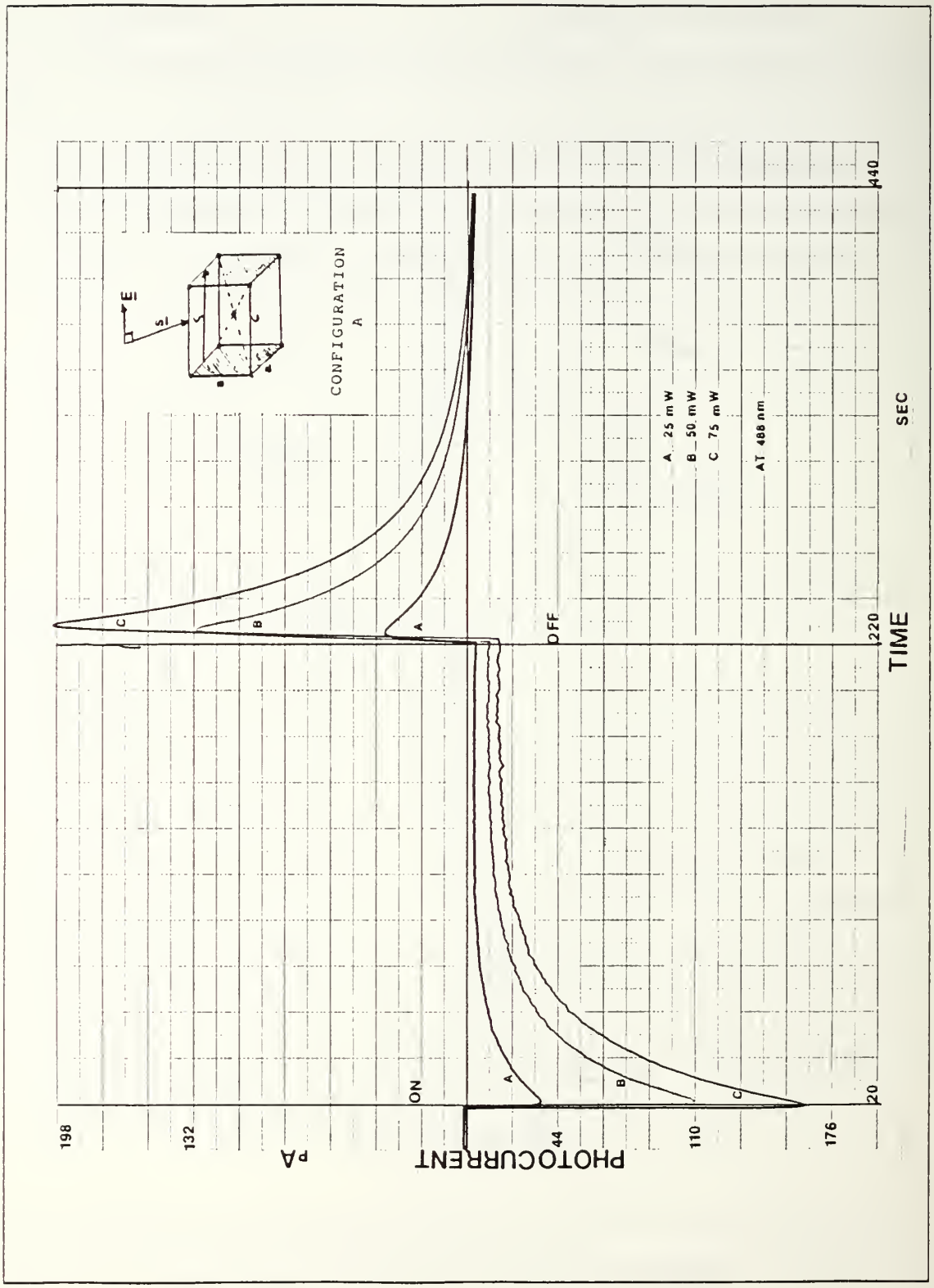

Figure 3.11 Measured photocurrent along -c axis.

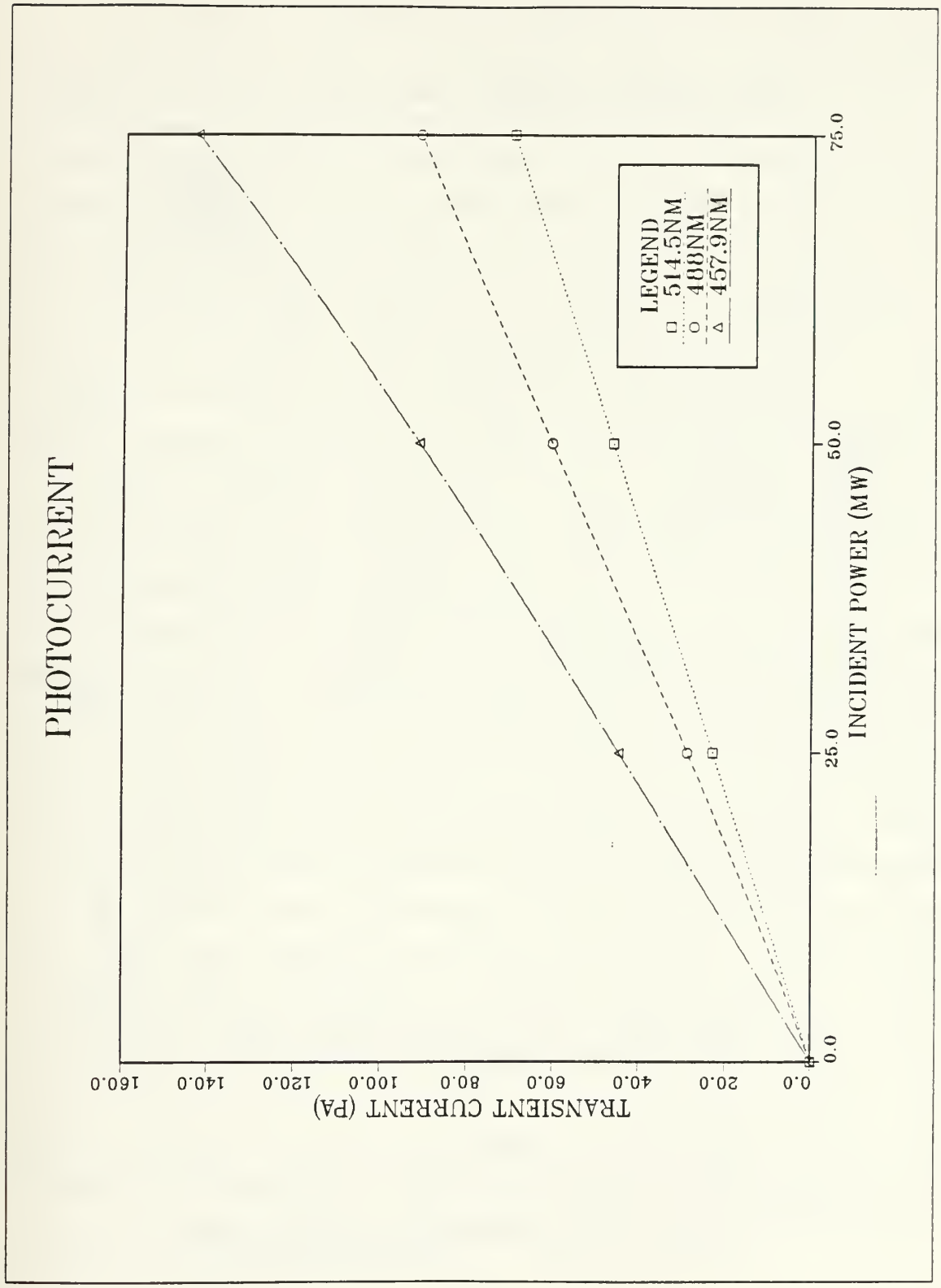

Figure 3.12 i_{py} (the pyroelectric current) versus incident power.

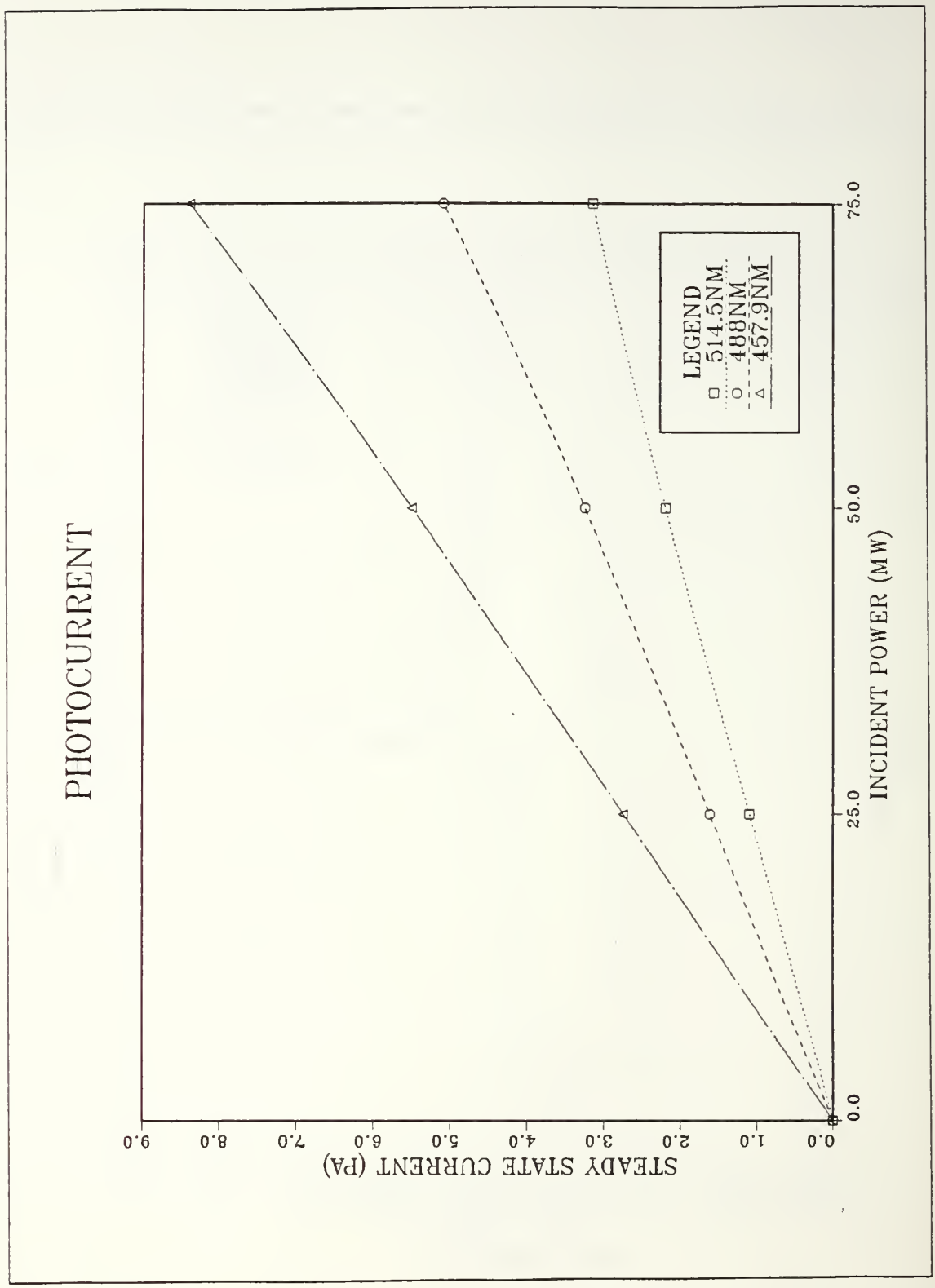

Figure 3.13 i_{ph} (SCPVC) versus incident power.

4. **Interpretation of the results**

Immediately, on unblocking the laser beam (ON positions in Figure 3.10 and 3.11), a high peak photocurrent (~ 100-200pA) was observed. The current, after the high peak showed a slow decay (50sec), eventually reaching a steady-state value of 1-9pA. On blocking the laser beam (OF position in Figure 3.10 and 3.11), there was an immediate transient current, 1.17 times larger than the initial transient current in magnitude and direction but in the opposite direction. This time the current decayed slowly to zero. We also observed that, when the c-axis direction was reversed, the polarity of the photo-induced currents reversed (see Figure 3.11). If we compare Figure 3.10 and 3.11, we see these differences: 1) The polarities of the photocurrents are different. 2) The amplitude of the photocurrents in Figure 3.11 is 1.6+/-0.3 times larger than the amplitude of the photocurrents in Figure 3.10. This is probably, because of absorption. The absorption coefficient in Figure 3.5 is 1.3 times larger than the absoption the absoprtion coefficient in Figure 3.6. This comparison suggests that the the higher absorption coefficient produced the higher peak current (see Figure 3.5 and 3.11). The large transient currents are pyroelectric in origin and the steady-state currents are BPVE in origin as will be explained below.

TRANSIENT CURRENT: When the laser beam is unblocked, the crystal temperature rises (~ 10°C), initially at the rate {(dT/dt) > 0}. This causes a pyroelectric current to flow, obeying Equation 2.12, along the c-axis al the crystal. The rise time of this current was ~ 200μ sec (see Figure 3.10 and 3.11). This can not be seen from the figures because the plotter response time was too slow. It was measured by a digital Nicolet oscilloscope. The rise-time was determined by the crystal capacitance (~ 25pF) and the crystal's internal RC equivalent circuit [Ref. 10]. As the temperature increased to its new steady-state value, (dT/dt) decreased. This caused the pyroelectric current to decay with a thermal relaxation time (40sec) to a steady-state value, which exists as long as the crystal was illuminated. In principle, when the crystal is at thermal equilibrium at the new temperature, then (dT/dt) was zero. This means that the pyroelectric current vanishes. But the steady-state current is not always zero (see next section). When the laser beam was blocked, the crystal started to cool down. At the beginning, its rate of cooling was maximum and then decayed slowly to zero. Eventually the crystal came into thermal equilibrium with the room temperature. This cooling down process is reflected in the current, which is in the direction opposite to the initial warming, because {(dT/dt) < 0}.

As mentioned earlier, photocurrent measurements were made at three wavelengths (514.5nm, 488nm, 457.9nm) and three different incident beam powers at each wavelength for two different crystal orientations. Figure 3.6 shows the peak transient current versus the incident beam power. We see that the transient current is linearly dependent on the incident beam power and it has wavelength dependence. In Figure 3.12, slopes of the lines are: 0.8 pA/mW at λ = 514.5nm, 1.2pA/mW at λ = 488nm and 1.6pA/mW at λ = 457.9nm.

STEADY-STATE CURRENT: This current is due to the bulk photovoltaic effect (BPVE) and is a result of anisotropic charge transport (see Section II-C). It existed as long as the crystal was illuminated by the laser beam. It shows up in Figure 3.6 and 3.7 as superimposed on the transient current (see Figure 3.10 and 3.11).

As we see from Figure 3.13, the short circuit photovoltaic current (SCPVC) is linearly dependent on intensity. Thus, this experimental observation verifies Equation 2.18 given in the thoery section. In Figure 3.13, slopes of the lines are: 0.044pA/mW at λ = 514.5nm, 0.06 at λ = 488nm and 0.11 at λ = 457.9nm. The SCPVC increased with frequency, which is consistent with the absorption coefficients in Equation 2.18. Previous experiments showed that the absorption coefficient increases with frequency. The SCPVC is only observed along the c-axis. This means that the field along the c axis of the crystal separate carriers. This statement is in complete agreement with Equation 2.17. In Figure 3.11, when the c-axis was reversed, the polarity of the SCPVC reversed (see Equation 2.15).

C. BEAM-COUPLING EXPERIMENTS

1. Purpose of this experiment

In order to calculate the quantum efficiency of $BaTiO_3$, we needed to know the charge transport length. We know that, theoretically, charge migration between traps cause, approximately a 90° phase shift between the hologram grating (index of refraction distribution) and the interference pattern (see Section II-G). This phase angle and the charge transport length can be calculated using the results of following experimental procedure.

2. Procedure

A Lexel Model 95 Ar^+ laser was used as a coherent light source. The output beam from this laser was vertically polarized. We needed a horizantally polarized beam for our purposes. Two quarter wave plates were used to accomplish this. As we see from Figure 3.14, beam splitter (BS) split the output beam into two equal intensity beams. One beam followed the path p1 (36cm) and mirror m2 reflected it back to the crystal, at an angle $\theta = 17.5°$ with respect to the crystal surface normal. Mirror m1, reflected the second beam onto mirror m3. This mirror reflected the second beam onto the crystal, making angle $\theta = 17.5°$ with the surface normal. The second beam path p2 was 33cm long. Two beams crossed each other at an angle $\sim$ 7° in the crystal (recall Snell's law). It was important to keep the difference in the path lengths (in our case p1-p2 = 3cm) of the two beams within the coherence length limit of the laser, which was about $\sim$ 6cm. Otherwise the interference pattern inside the crystal could not occur. The intensity of the first beam was 1/2 of the second beam (A = 0.5). Initially, the two beams were kept on the crystal until the grating was established. Then the strong beam was blocked to determine the energy transfer from the strong beam to the weak beam.

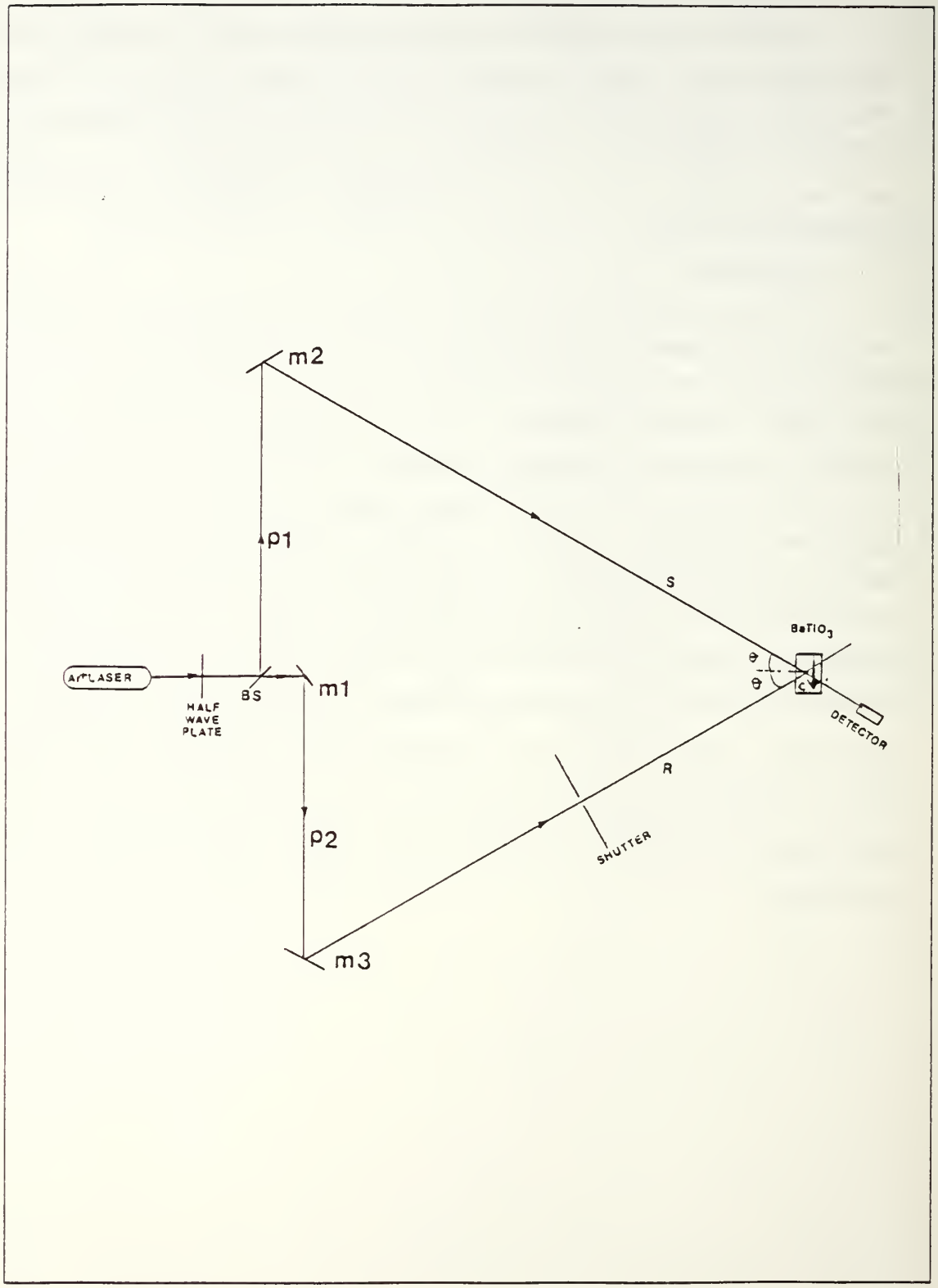

Figure 3.14 Experimental set-up for beam-coupling..

3. Results of the experiments

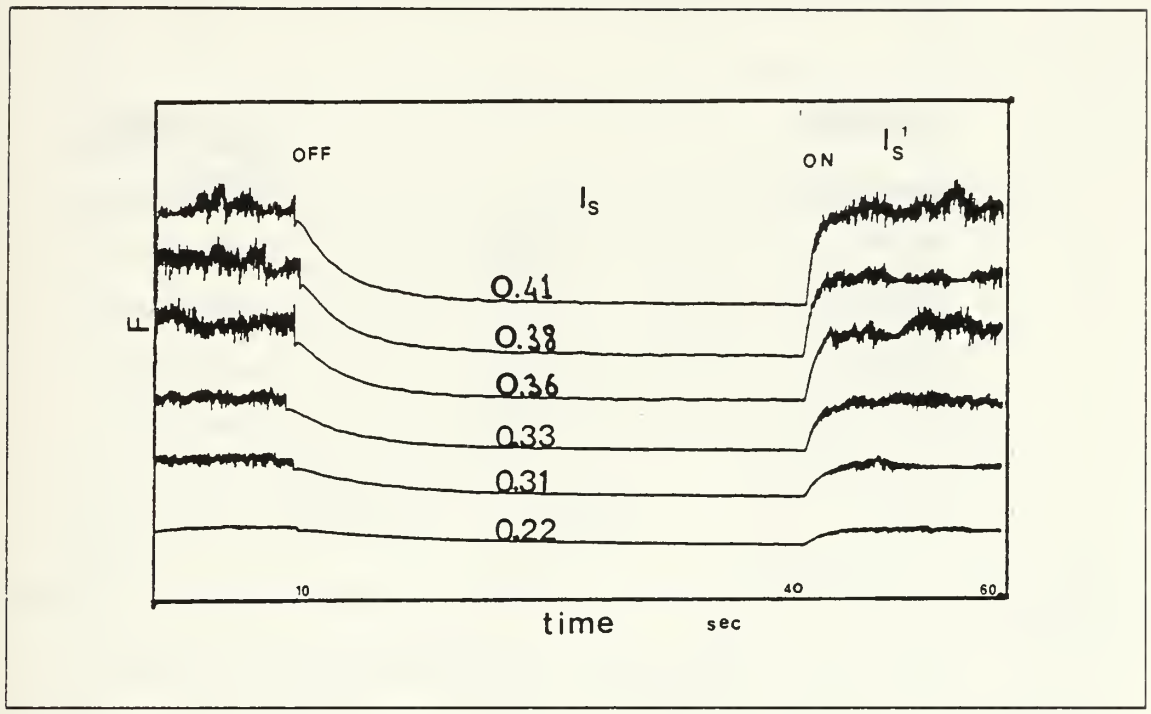

Figure 3.15 The fractional energy transfer (F) at λ = 488nm.

The numbers on the curves denote the fractional energy transfer (F). The I_s is the intensity of the signal beam when the reference beam was turned off. The I_s^1 is the intensity of the signal beam when the reference beam was turned on.

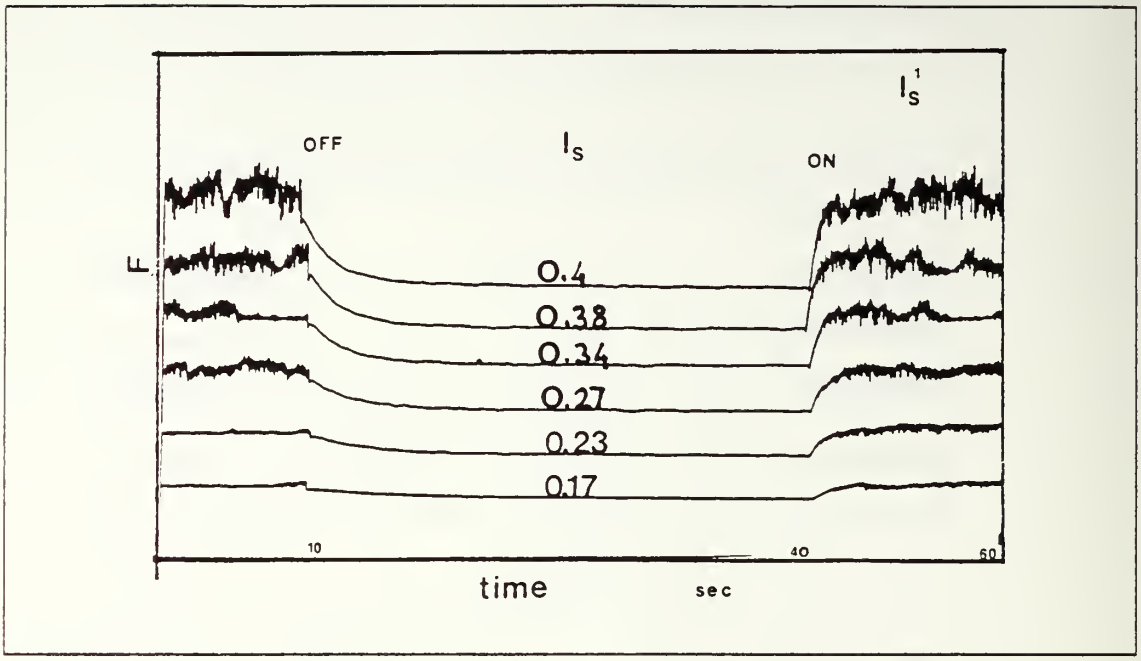

Figure 3.16 The fractional energy transfer (F) at λ = 457.9nm.

The numbers on the curves denote the fractional energy transfer (F). The I_s^1 is the intensity of the signal beam when the reference beam was turned on. The I_s is the intensity of the signal beam when the reference beam was turned off.

4. **Interpretation of the results**

As is shown in Figure 3.15 and 3.16, when the strong beam was blocked (OFF conditions in the figures), the intensity of the weak beam decreased and reached a steady-state value I_s . After 10 seconds, the strong beam was unblocked (ON positions in the figures), and the intensity of the weak beam increased and reached a steady-state value I_s^1 . This is the manifestation of energy transfer in beam-coupling. Energy transfer occurs, because the refractive index grating (hologram grating) scatters the two beams that produce it. Using Equation 2.53 and the data obtained from the beam-coupling experiments, the diffraction efficiency of the hologram grating was calculated. Figure 3.17 shows the diffraction efficiency versus wavelength of the laser beam. The direction of energy transfer is determined by the direction of the c-axis of the crystal and the phase shift angle. According to Valley [Ref. 24], the direction of energy transfer depends on the type of carrier which dominates in charge transport. In our experimental set-up, the strong beam enters the crystal at the -c-axis edge and beam-

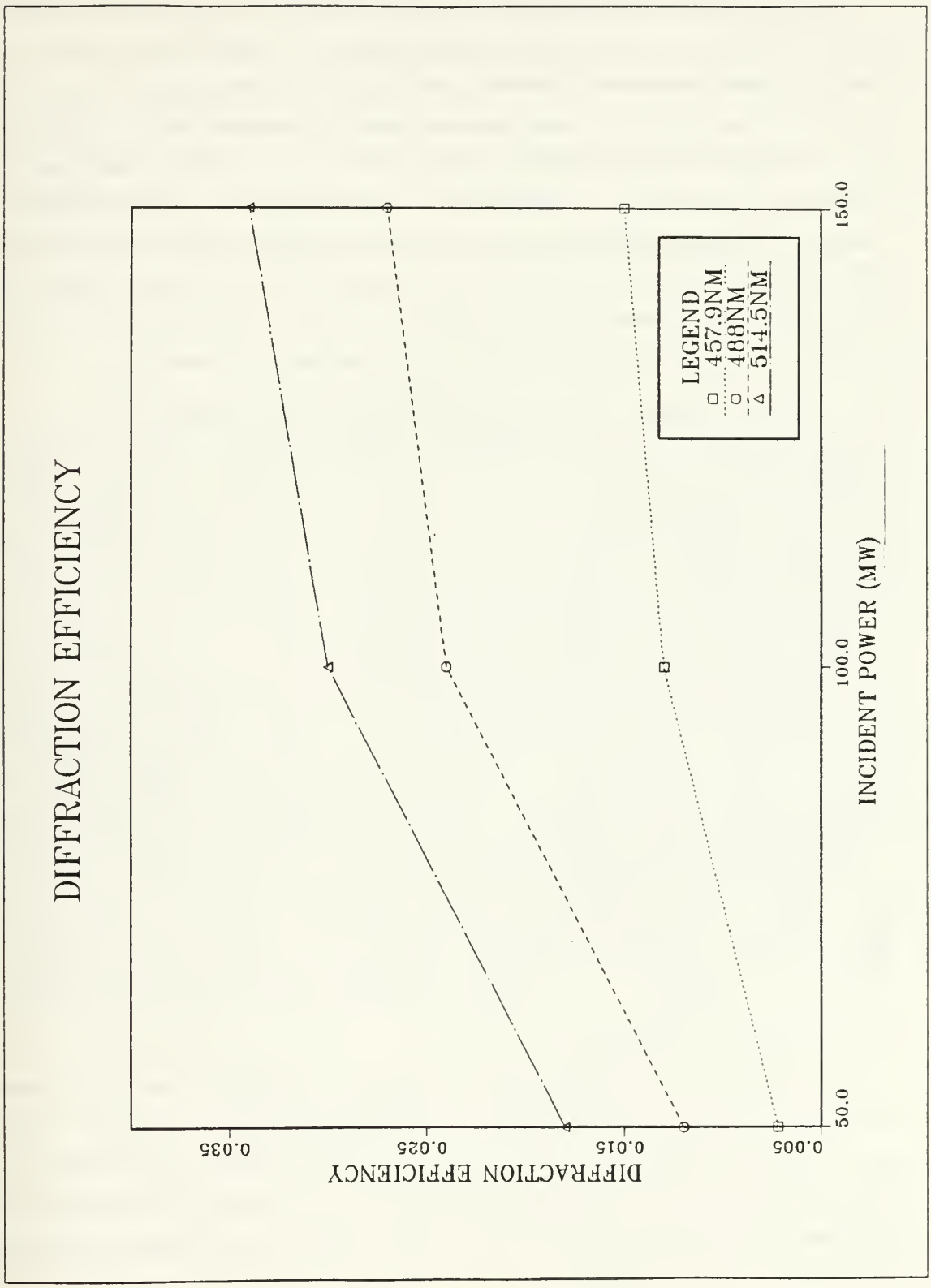

Figure 3.17 Diffraction efficiency vs wavelength.

coupling occurs in the +c direction. This means that in our crystal, the majority carriers are electrons (according to Valley's theory). Our observations agree with Gunter's [Ref. 38] arguments. These arguments are: 1) Energy transfer occurs only if the two writing beams have different intensities. In our experiment, $A = I_s / I_r = 0.5$. 2) Energy is always transferred from the strong beam to the weak beam. 3) If $|\varphi_0 - \varphi| > \pi / 2$, where φ_0 is the phase difference between the two beams and φ is the phase shift of the index grating from the intensity pattern, then the energy transfer is oscillatory. In our experiments, the difference between the path lengths of the two beams was 3cm. This distance introduced a phase difference between the two incident beams. This is why, we observed an oscillatory response under steady-state conditions in Figure 3.15 and 3.16. As the path difference increased, the oscillations increased.

D. CALCULATION OF THE QUANTUM EFFICIENCY OF $BATIO_3$

In this section, the quantum efficiency of $BaTiO_3$ will be calculated, using the experimental data and the equations derived in Section II-H. In Section III-B, the pyroelectric current was given, this data will be used to calculate the photorefractive absorption coefficient. Using Equation 2.66 and the measured value of the pyroelectric current we found the photorefractive absorption coefficient α_p . For example, at $\lambda = 488$nm, the measured value of the pyroelectric current was $i_{py} = 27.26$pA (see Figure 3.12). Using Equation 2.66, the photorefractive absorption coefficient was found to be $\alpha_p = 0.0086\text{cm}^{-1}$ for the beam power 25mW at $\lambda = 488$nm. Similar calculations were made at $\lambda = 514.5$nm and $\lambda = 457.9$nm for three different incident beam powers (25mW, 50mW, 75mW). Figure 3.17 shows the photorefractive absorption coefficient versus wavelength of the laser beam. The absorption coefficients were measured by the spectrophotometer (for example, see Figure 3.3) have the same wavelength dependence with Figure 3.17. The comparison between the α and the α_p shows that the photorefractive absorption coefficient is approximately 200 times smaller than the absorption coefficients were found in Section III-A. For example, from the spectrophometric measurement the absorption coefficient was found to be $\alpha = 2\text{cm}^{-1}$ at $\lambda = 457.9$nm. The photorefractive absorption coefficient from the pyroelectric current measurements was found to be $\alpha_p = 0.013\text{cm}^{-1}$ at $\lambda = 457.9$nm. Moreover, since Glass [Ref. 39] has shown that the photo-induced change in the refractive index is strongly dependent on the incident beam intensity and since α_p was measured here is dependent on the incident beam power, we have clear causal connection between our measured α_p and photorefraction.

As stated in Section II-B, the anisotropy constant κ is the measure of the difference between the probabilities of exicitation and recombination along the +c and -c axes of the crystal. The anisotropy constant is needed to calculate the quantum efficiency. Using Equation 2.68 and the experimentally measured values of the SCPVC (see Figure 3.13), the anisotropy constant were calculated. For example, at λ = 488nm the measured value of the absorbed power was $\Phi = 2.15*10^{-4}$ Watt/cm, using i_{py} = 27.26pA in Equation 2.66 and a measured value of SCPVC was i_{ph} = 1.62pA (see Figure 3.13). Putting these numbers in Equation 2.68 the anisotropy constant was found to be $\kappa = 0.39*10^{-9}$ A cm /Watt. Similar calculations were made at λ = 514.5nm and λ = 457.9nm for three different incident beam powers (25mW, 50mW, 75mW). In Figure 3.18, the anisotropy constant is plotted versus wavelength. The phase shift angle φ_{ph} is the last parameter involved in the calculation of the quantum efficiency. Using the measured value of the fractional energy transfer (see Figure 3.15 and 3.16), M (from Equation 2.49) and A = 0.5 in Equation 2.70, φ_{ph} was calculated. At λ = 488nm, the measured value of the fractional energy transfer was F = 0.22 (see Figure 3.15), M = 12.57 (from Equation 2.49) and the intensity ratio of the signal and the reference beams was A = 0.5. Using Equation 2.70, the phase shift angle was found to be φ_{ph} = 52.1°. Similar calculations were made at λ = 514.5nm and at λ = 457.9nm. Figure 3.20 shows the phase shift angle φ_{ph} versus wavelength. Using the values of the anisotropy constant (from Figure 3.19), the phase shift angle (from Figure 3.20) and the wave number of the the hologram grating ($K = 4*\pi \sin\theta / \lambda$) in Equation 2.72, the quantum efficiency was calculated. For example, at λ = 488nm, the value of the anisotropy constant was $\kappa = 0.39*10^{-9}$ A cm/W, the value of the phase shift angle was 52.1° and the wave number of the hologram grating was $K = 8.25*10^{6}$ m. Using Equation 2.72, the quantum efficiency of $BaTiO_3$ was found to be $5.96*10^{-5}$. Similar calculations were made at λ = 514.5nm and at λ = 457.9nm. Figure 3.21 plots the quantum efficiency is plotted versus wavelength.

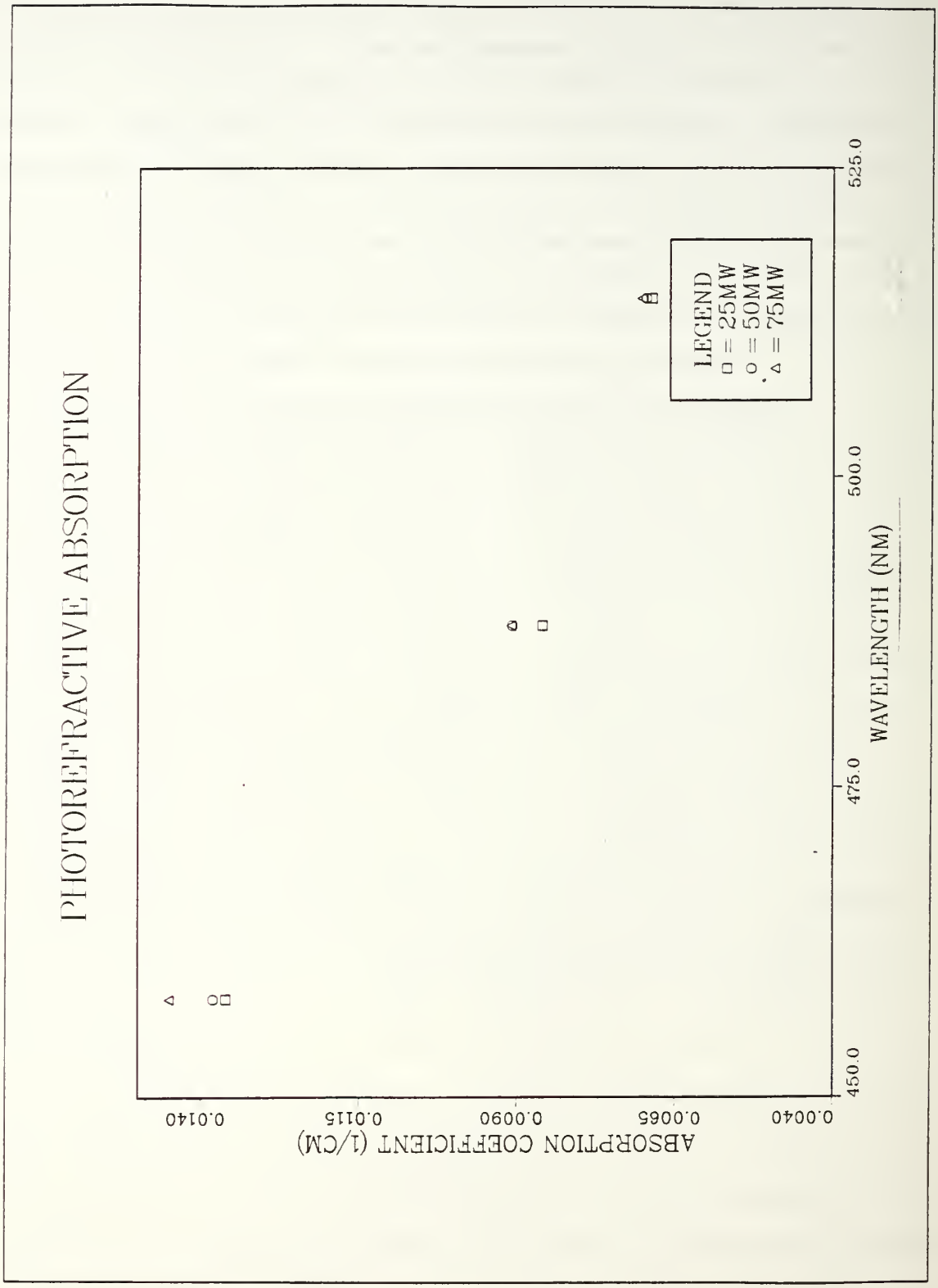

Figure 3.18 Photorefractive absorption coefficient of $BaTiO_3$.

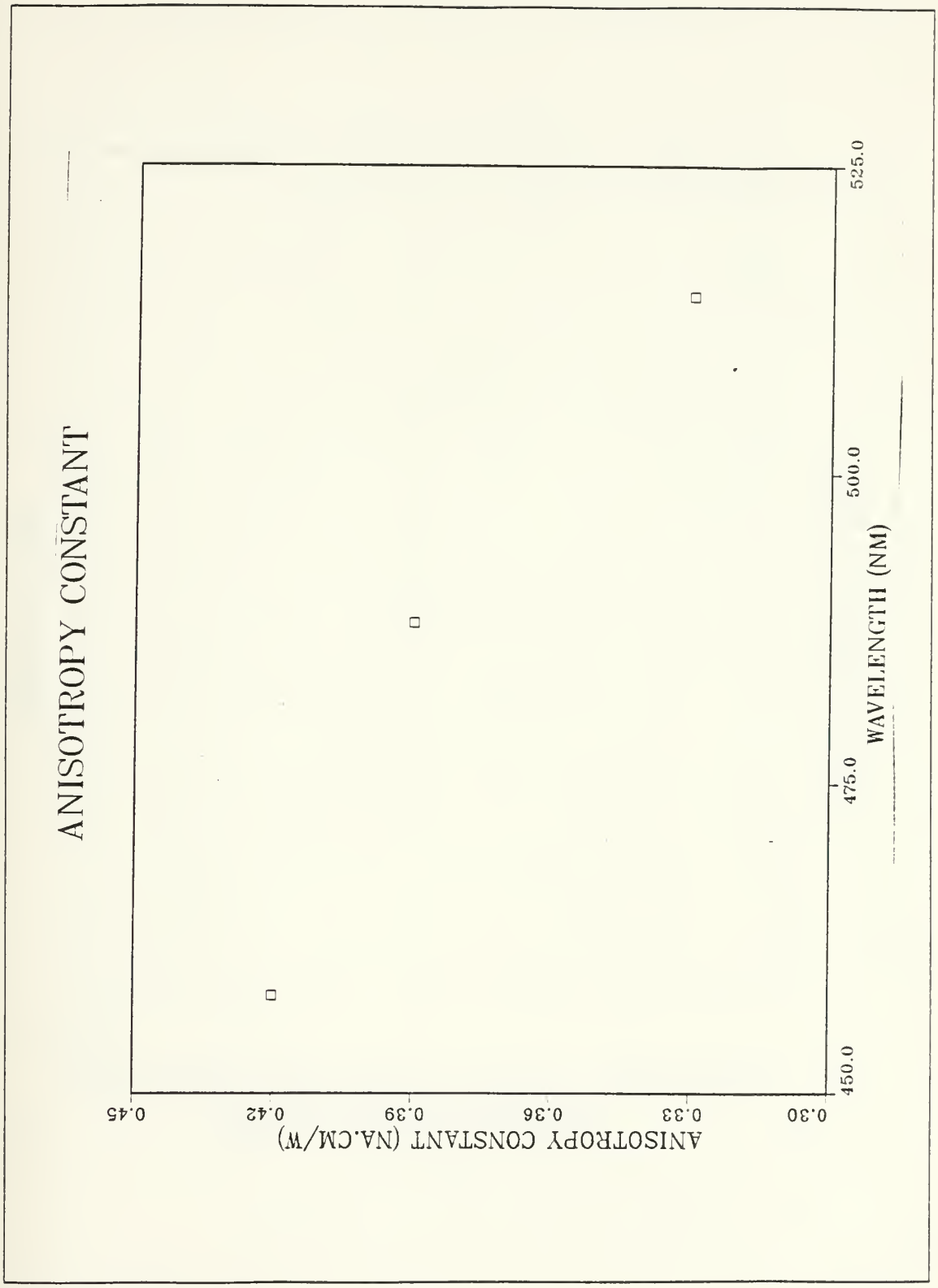

Figure 3.19 Anisotropy constant of $BaTiO_3$.

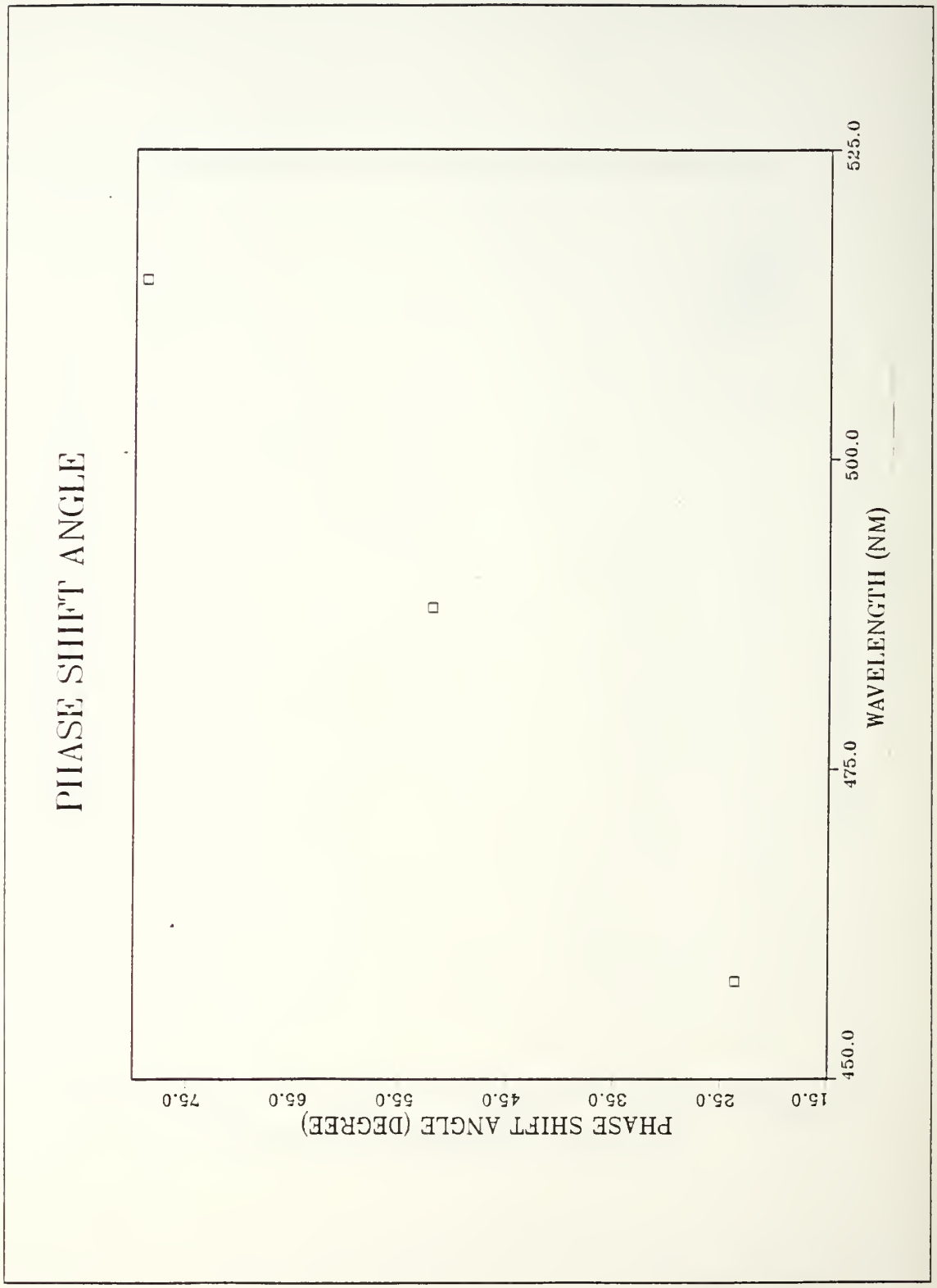

Figure 3.20 Phase shift angle between gratings.

Figure 3.21 Quantum efficiency of $BaTiO_3$.

E. DISCUSSIONS

This section summarizes the photorefractive effect in $BaTiO_3$ quantitatively. This will be done with a two beam-coupling example at one wavelength. At $\lambda = 457.9$nm, the wave number of the intensity interference pattern was $K = 8.25*10^6$ m ($K = 4*\pi \sin\theta / \lambda$, where $\theta = 17.5°$ is angle with crystal surface normal). If $3.9*10^{14}$ photons per sec were absorbed (from Equation 2.63 for the value of the absorbed power $\Phi = 1.72*10^{-4}$ Watt/cm), photo-carriers (in our case electrons are majority) will be freed from the absorption centers (see Section II-E) Under the influence of BPVE (see Section II-H), carriers will migrate from the illuminated regions to the dark regions. This process sets-up a space charge field, since we assumed a one dimensional charge transport (c-axis direction) in Section II-C. Using the measured value of the fractional energy transfer $F = 0.17$ (see Figure 3.15), $A = 0.5$ (the beam ratios) and $M = 10.06$ (from Equation 2.49) in Equation 2.70, the phase shift angle was found to be $\varphi_{ph} = 23.72°$. With this value of the phase shift angle in Equation 2.71, the charge transport length was found to be 53nm. Using the measured value of the fractional energy transfer $F = 0.17$ in Equation 2.53, the diffraction efficiency of the hologram grating was found to be $\eta = 0.0072$. Using this value of diffraction efficiency and a 3.6mm hologram grating ($l = t/\cos\theta$) in Equation 2.49, the amplitude of refractive index change was found to be $\delta n_{33} = 2.45*10^{-6}$. Using from Table 1 the values of the extraordinary index of refraction $n_3 = 2.365$ and the electrooptic coefficient along the c-axis of the crystal $r_{33} = 23*10^{-12}$ m/V and the value of the refractive index change in Equation 2.41, the magnitude of the space charge field was found to be 16.11 kV/m. The quantum efficiency of $BaTiO_3$ at this wavelength was found to be $2.13*10^{-4}$ (see Figure 3.21). Using this value of the quantum efficiency in Equation 2.29, the the generation rate of electrons was $8.3*10^9$ per sec. If we consider the density of photorefractive center as 10^{16} cm^{-3} [Ref. 19], then in a volume of $6.6*10^{-3}$ cm^3 ($A_b = 0.0132cm^2$ and $t = 0.5$cm) $6.6*10^{13}$ electrons were found. Glass et al. [Ref. 31] found the quantum efficiency of $LiNbO_3$ as 0.17, this value of the quantum efficiency gave a electron density that was three times the density of the photorefractive center, which is impossible. Our calculation of the quantum efficiency gave a value of the electron density (see above photo-excited electron density is smaller than the impurity density) that is consistent with the density of oxygen vacancies.

IV. CONCLUSIONS

The fact that the absorption coefficients, measured in the visible region of the spectrum, were found to be different for each of the six crystal orientations shows that the absorption centers are distributed anisotropically in the crystal. From these measurements, the band gap of $BaTiO_3$ was found to be E_g (1) = 3.08eV and E_g (2) = 3.15eV. A broad plateau was observed between 880nm and the band edge at 460nm. This was due to the low oxygen pressure used during crystal treatment. In the infrared region of the spectrum, a broad band 8-15μ m was observed and this comes from stretching vibrations of TiO_3 atoms. At λ = 500nm the maximum absorption coefficient was α = 2.32cm^{-1} and the minimum absorption coefficient was α = 0.88cm^{-1} . These numbers are too large to be accounted by the photorefractive absorption centers alone. Since Glass [Ref. 39] has shown that the photo-induced change in the refraction index is strongly dependent on the incident beam intensity and since our measurements of the photorefractive absorption coefficient α_p were dependent on the incident beam power, this suggests the causal connection between our measuement of α_p and photorefraction (see Figure 4.1 and 3.18).

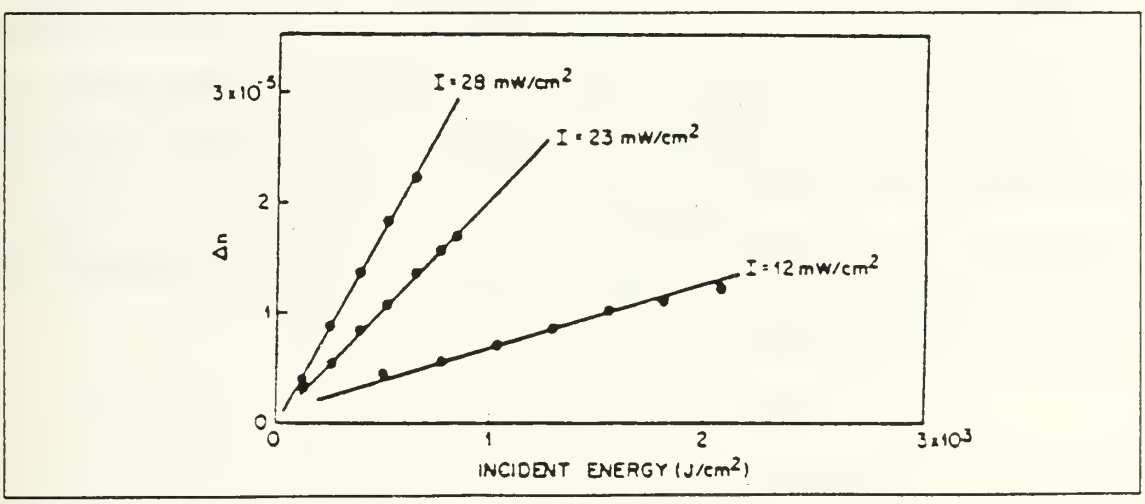

Figure 4.1 Intensity vs the index of refraction change [Ref.39].

The photorefractive absorption coefficient were determined from the pyroelectric current measurements. The maximum value of the photorefractive absorption

coefficient was found to be $\alpha_p = 0.0145 cm^{-1}$ at $\lambda = 457.9 nm$ for a beam intensity of 75mW. The minimum value of α_p was found to be $0.0086 cm^{-1}$ at $\lambda = 488 nm$ for a beam intensity of 25mW. We see that the photorefractive absorption coefficient is ~ 200 times smaller than the absorption coefficient obtained from the spectrophotometric measurements. This important point has been overlooked previously in the literature. From the short circuit photovoltaic current (SCPVC) and the absorption coefficients derived from the pyroelectric current measurements, the anisotropy constant was found to be $\kappa = 0.4*10^{-9}$ (Ampere.cm/watt) at $\lambda = 457.9 nm$. With this information the quantum efficiency times charge transport length was found to be $QL_{ph} = 1.13*10^{-9}$ cm. From beam-coupling experiments, the amount of fractional energy transfer between two beams was found to be ~ $F = 0.18$. Combining this information with the results of coupled wave theory, the diffraction efficiency of a hologram grating was found to be $\eta = 0.018$ at $\lambda = 514.5 nm$. The maximum value of the phase shift angle between the hologram grating and the intensity pattern at $\lambda = 514.5 nm$ was 78.9°. The minimum charge transport length in photovoltaic process was $L_{ph} = 53 nm$. The quantum efficiency increases with the frequency of incident light. The maximum value of the quantum efficiency was $Q = 2.13*10^{-4}$ (at $\lambda = 457.9 nm$), and the minimum value of the quantum efficiency was $Q = 1.13*10^{-5}$ (at $\lambda = 514.5 nm$). For absorption of $3.9*10^{14}$ photons per sec at $\lambda = 457.9 nm$ and with this value of the quantum efficiency, the generation rate of electrons was $8.3*10^{10}$ per sec. If the density of absorption centres is 10^{16} cm^{-3} , then in the volume occupied by the beam in the crystal ($6.6*10^{-3}$ cm^3), there are $6.6*10^{13}$ electrons. Young et al. [Ref. 32] found the quantum efficiency of $LiNbO^3$ as $Q = 2*10^{-3}$ and the charge transport length as $L_{ph} = 50 nm$ (wavelength was not given in the literature). But they used the large values for the absorption coefficient. This compares well the quantum efficiency of $BaTiO_3$ as $Q = 2.13*10^{-4}$ and the charge transport length as $L_{ph} = 53 nm$ at $\lambda = 457.9 nm$ that we found. Since the lifetimes of the carriers are still unknown, the Dember effect can be used to determine the lifetimes in future measurements.

LIST OF REFERENCES

1. Chen, F.S., J.Appl.Phys., 40, 3389, (1969)

2. Kukhtarev, N.V., Markov, V.B., Odulov, S.G., Soskin, M.S., Vinetskii, V.L Ferroelectrics, 22, 949, (1979)

3. Jona, F., Shirane, G., Ferroelectric Crystals, Pergamon Press, (1962)

4. Kittel, C., Introduction to Solid State Physics, Sixth Edition, Wiley (1986)

5. Devonshire, A.F., Phil.Mag., 40, 1040, (1949)

6. Slater, J.C., Phys. Rev., 78, 748, (1950)

7. Merz, W.J., Phys. Rev., 76, 1221, (1949)

8. Chynoweth, A.G., J.Appl.Phys., 27, 78, (1956)

9. Eustace, L.D., Devon, G.C., Optical Radiation Detectors, Wiley (1984)

10. Chynoweth, A.G., Phys.Rev., 102, 705, (1956)

11. Glass, A. M., Appl.Phys.Lett., 25, 233, (1974)

12. Gower, M.C., Opt.Lett., 11, 458, (1986)

13. Brody, P. S., Sol.St.Comm., 12, 673, (1973)

14. Koch, W.T.H., Munser, R., Ruppel, W., Wurfel, W. Sol.St.Comm., 17, 847, (1975)

15. Bube, R.H., Photoconductivity of Solids, Wiley (1960)

16. Glass, A.M., Chanussot, G., Phys.Lett , 59A, 405, (1976)

17. Baltz, R.Von., Kraut, W., Sol.St.Comm., 26, 961, (1978)

18. Klein, M.B., Schwartz, R.N., J.Opt.Soc.AmB. , 3, 293, (1986)

19. Feinberg, J., Ducharme, S., J.Opt.Soc.AmB. 3, 283, (1986)

20. Hellwarth, R.V., Strohkendl, F.P., Jonathan, J.M.C., Opt.Lett., 15, 313, (1986)

21. Young, L., Moharam, M.G., J.Appl.Phys., 48, 3230, (1977)

22. Feinberg, J., Heiman, D., Tanguay, A.R., Helwarth, R.W. J.Appl.Phys., 51, 1297, (1980)

23. Young, L., Moharam, M.G.M., Gaylord, T.K., Magnusson, R. Ferroelectrics, 27, 255, (1980)

24. Valley, G.C., J.Appl.Phys., 59, 3363, (1986)

25. Yariv, A., Quantum Electronics, Second Edition, Wiley, (1985)

26. Johnston, D., J.Appl.Phys., 41, 3279, (1970)

27. Vahey, W.D., J.Appl.Phys., 46, 3510, (1975)

28. Young, L., Moharam, M.G., Gaylord, T.K., Magnusson, R. J.Appl.Phys. 50, 5642, (1979)

29. Kogelnik, H., Bell.Syst.Techn.J., 48, 2909, (1969)

30. Amodei, J.J., Staebler, D.L., J.Appl.Phys., 43, 1042, (1972)

31. Glass, A.M., Peterson, G.E., Negran, J.T., An Introduction to Electrooptic Devices. Kaminow, I.P., Academic Press. 325, (1974)

32. Young, L., Moharam, M.G., Guibaly, F.E., Lun, E., J.Appl.Phys. 50, 4201, (1979)

33. Kratzig, E., Orlowski, R., Opt.Qm.Eln., 12, 495, (1980)

34. Young, L., Moharam, M.G., Guibaly, F.E., Lun, E. J.Appl.Phys., 50, 4201, (1979)

35. Vahey, W.D., J.Appl.Phys., 46, 3510, (1975)

36. Casella R.C., Keller, S.P., Phys.Rev., 15, 1469, (1959)

37. Last, J.T., Phys.Rev., 105, 1740, (1956)

38. Gunter, P., Phys.Rep., 93, 199, (1982)

39. Glass, A.M., Opt.Eng., 17, 470, (1980)

INITIAL DISTRIBUTION LIST

		No. Copies
1.	Defense Technical Information Center Cameron Station Alexandria, Virginia 22304-6145	2
2.	Library, Code 0142 Naval Postgraduate School Monterey, California 93943-5000	2
3.	Donald L. Walters Code 61 We Naval Postgraduate School Monterey, California 93943	10
4.	Nathaniel E. Glass Code 61 Gc Naval Postgraduate School Monterey, California 93943	1
5.	Gazanfer Unal Kaptan Arif Cad Coban Yildizi Sok No=26/19 Erenkoy Istanbul Turkey	4
6.	Deniz Harp Okulu Kutuphanesi Tuzla Istanbul Turkey	1
7.	Bogazici Universitesi Kutuphane Bebek Istanbul Turkey	1

89
18070 2

Thesis
U353 Unal
c.1 Measurements of the microscopic properties contributing to photorefraction in barium titanate.

thesU353
Measurements of the microscopic properti
3 2768 000 70972 9
DUDLEY KNOX LIBRARY